Neat and Aqueous Polyelectrolytes under a Steady-Shear Flow

Patrick A. Bonnaud,[*,†,‡] Hiroshi Ushiyama,[†] Syogo Tejima,[†] and Jun-Ichi Fujita[¶]

†*Research Organization for Information Science and Technology, Department of Computational Science and Technology, 1-18-16 Hamamatsucho, Minato, 105-0013, Tokyo, Japan.*

‡*University of Tsukuba, 1-1-1 Tennodai, Tsukuba, Ibaraki, 305-5875, Japan.*

¶*Institute of Applied Physics, Graduate School of Pure and Applied Science, University of Tsukuba, 1-1-1 Tennodai, Tsukuba, Ibaraki, 305-8573, Japan*

E-mail: bonnaud@rist.or.jp

Phone: +81-03-6433-0670

Abstract

Materials enabling impact-energy absorption of high-velocity projectiles are of great interest for applications like aerospace. In such a frame, shear-thickening fluids were found very useful. Here, we investigated nano-rheological properties of neat and aqueous polyelectrolytes of low molecular weights containing poly([2-(methacryloyloxy) ethyl] trimethyl ammonium) as polycations and poly(acrylamide-co-acrylic acid) as polyanions. Results were compared with pure water. We employed Non-Equilibrium Molecular Dynamics with the SLLOD algorithm to compute the viscosity at various shear rates. Systems containing polyelectrolytes exhibit shear thickening. The analysis of molecular configurations revealed a strong disruption of the ionic structure and more clusters with smaller sizes when raising the shear rate. Potential energies showed that shear thickening originates from an increase in intramolecular and van der Waals interactions resulting from the increasing difficultly of polyelectrolyte-based systems to relax at high shear rates. Our method and findings underscore the importance of accounting for the molecular scale in the design of materials absorbing the impact energy efficiently.

Introduction

Smart, structural materials resisting external mechanical stimuli like impacts ensure the integrity of structures and encounter various applications ranging from aeronautics to aerospace, protective clothing (e.g., body armours), and sports equipment (e.g., tennis rackets).[1–4] Some of them involve high-impact velocities (e.g., gun bullets or space debris) with values ranging from hundreds to thousands of m/s.[5–8] For such applications, shear thickening fluids (STFs) as non-Newtonian fluids are of great interest, because of their ability to absorb the kinetic energy transferred to structural materials upon collisions (or high-shear rates) through a dramatic increase of the shear viscosity.[1,2,4] In the case of protective clothing, STFs offer the possibility of a full body protection with a better flexibility of the wearer for a nor-

mal range of movements due to their liquid state at rest.[1] Pinto et al.[2] found up to 45% of energy absorption during an impact event at 2.5 m/s for silica-particle-based polymer mixtures. STFs are made of a dispersed phase (colloids or particles) in a continuous, liquid phase, i.e., a colloidal dispersion.[2,4] Parameters affecting the shear-thickening effect are the concentration, the nature (i.e, organic, inorganic, and surface chemistry), and interactions among elements of the dispersed phase.[2,9] From an industrial purpose, the concentration of colloids is a parameter that has to be chosen carefully in order to find the best compromise between workability of the fluid and viscosity requirements.[2] Depending on the colloid nature, one can encounter different mechanisms at the origin of shear thickening. For inorganic colloids like silica particles, we expect an order-disorder transition thickening the fluid and, thus, increasing the viscosity through the formation of hydroclusters.[2,4] At low shear rates, colloids arrange themselves in ordered layer facilitating their flow (i.e., straight flow path), which reduces viscosity.[2] They aggregate in clusters under high-shear rates due to tortuous flow paths, which thickens the fluid (i.e., dilatancy).[2] The transition between the two aforementioned behaviors is classically defined by $\dot{\gamma}_c$, the critical point at which viscosity starts to rise when raising the shear rate ($\dot{\gamma}$).[1,2] The higher the temperature, the higher the critical shear rate from which shear thickening occurs, and the lower the viscosities.[4] The higher the volume fraction of colloids, the lower the critical shear rate, and the more intense the shear thickening effect.[4] Interestingly, Brown et al.[10] showed that the yield stress can mask shear thickening in colloidal suspensions, but reducing the yield stress below a threshold allow recovering dilatancy. As a matter of fact, because shear thickening is attributed to general mechanisms like hydrodynamics or dilation,[4,10] all suspensions are expected to yield shear thickening under the right conditions.[10]

Polymer melts and aqueous solutions also exhibit a non-Newtonian behavior. Those mixtures mostly display shear thinning,[11–13] but, even if less common, a shear thickening effect can be encountered.[12,14] Bokias et al.[14] reported that in most cases shear thickening is not very pronounced and appears only at rather low shear rates. As a general trend, the overall

rheological behavior of polymer aqueous solutions is driven by both the polymer concentration[14] and microstructure,[12,15] since they determine the nature and the ability of forming inter- and intra-chain junctions (usually reversible) for polymer macromolecules in aqueous media.[14,15] In such a way, flexible-backbone (block) copolymers with amphiphilic properties were synthesized over the past decades in order to have water-soluble entities.[15,16] Usually, water-soluble polymers are modified in order to contain a small number of hydrophobic groups.[12] Those hydrophobically modified polymers allow the formation of interchain aggregates driven by hydrophobic interactions for concentrations high enough, yielding the formation of a transient network (gelation) and, thus, an enhanced viscosity (thickening) competing with those observed for higher molecular weight homopolymers.[12,14] For too low concentrations, intrachain aggregates form in a given polymer macromolecule among its hydrophobic sections lowering the viscosity of aqueous solutions.[14,15] Furthermore, the hydrophobic group distribution in polymer chains (microstructure) significantly affects the associative behavior among molecules.[12,15] Whereas a random distribution favors intramolecular associations, sequences of several consecutive hydrophobic units (microblocks) in polymer molecules favors intermolecular associations given a concentration high enough.[15] The effective lifetime of reversible junctions governs the system dynamics.[14] Under increasing shear, reversible junctions among polymer chains break, leading usually to shear thinning (reduced viscosities).[12,14] When the shear decreases, physical links among chains reform.[12,14]

Shear thickening was also observed for aqueous solutions of polymers.[11,14,15,17,18] It originates from the formation of interchain complexes (cross-linked networks)[11,14,17,18] among polymer molecules having few localized, energetically favored interactions in their carbon backbone.[18] The elongation of polymer molecules under shear[17] and the increase of the collision frequency between groups of different polymer chains[11] promote shear thickening. In such a way, Takeda et al.[19,20] showed that aqueous polyelectrolytes containing solely hydrophilic species like poly([2-(methacryloyloxy) ethyl] trimethyl ammonium)[21] for polycations (PC) and poly(acrylamide-co-acrylic acid)[3,12,16,22–26] for polyanions (PA) exhibit di-

latancy. In their experiments,[19,20] molecular weights were 70-80 kg/mol and ∼150 kg/mol for PC and PA, respectively. Coulomb interactions needed to be engineered with care, since too strong attractive forces between solvated PC and PA results in aggregation (or flocculation).[10,19,20] Whereas each monomer in PC carry a partial charge, PA are made of neutral monomers (i.e., mainly acrylamide monomers) with randomly distributed charged monomers (i.e., acrylic acids with an unsaturated oxygen).[19,20] 97% of the monomers constituting PA macromolecules are acrylamide ones.[19,20] Macromolecules were dissolved in water at a PC:PA mole ratio 1:4 and stand for ∼0.05 wt.% of the total solution. From their rheological experiments at the macroscale, authors explained the observed dilatancy through the formation of a homogeneously distributed network of PA with PC acting as local binders.[19,20]

Those peculiar results were the cornerstone of our current research approach, where the ultimate aim is to provide a full molecular-scale understanding of the shear-thickening mechanism in aqueous polyelectrolytes with molecular simulations. We focused our study on steady-shear flow, since impacts of projectiles can be seen as indentation experiments performed at high velocity, where shear mechanisms dominate[27] for materials having high values of Poisson's ratio like polyelectrolytes. We started with systems containing short PC and PA molecules (i.e., low molecular weights), where charges are highly concentrated in the polymer chain, at a 1:1 mole ratio mixed with water or not and compared our results with pure, bulk water. The formation of a network of interchain bindings at high shear rates is very unlikely to happen with such small molecules. Shear thickening occurs through a different mechanism. After presenting our methods for building molecular models and simulating systems, we show and discuss our results on nano-rheological properties. These results and approaches will enable the simulation of longer polymer chains as well as various chemical compositions of PA and PC.

Methods

Generation and equilibration of molecular models

To model PC and PA molecules, we first generated monomers of [2-(methacryloyloxy) ethyl] trimethyl ammonium, acrylamide, and acrylic acid, where radicals R_1 and R_2 are explicitly described, i.e., geometrical sites used to connect monomers. Snapshots of molecular structures were obtained with the VMD software[28] and reported in Fig. 1. We used those monomers as building blocks in our homemade code relying on pure geometric criteria to connect them between each other and, then, to form longer polymer chains (see molecular models in Fig. 2). We allowed the monomers to rotate slightly around the covalent bond that links them together in order to avoid overlapping atoms. We considered $N = 3$ monomers of acrylamide and $M = 3$ monomers of acrylic acid to generate a PA molecule and $K = 3$ monomers of [2-(methacryloyloxy) ethyl] trimethyl ammonium for a PC molecule. Monomers were randomly inserted in the carbon backbone of the PA molecule and only one molecule was generated. Thus, in configurations containing many molecules, charged monomers have always the same location in the polymer chain. Final molecular weights (M_w) for PC and PA molecules were $\sim$518.72 and $\sim$428.39 g/mol, respectively, which is two to three orders of magnitude lower than experimentally.[19,20]

In our Molecular Dynamics (MD) approach, we have considered the General Amber Force Field (GAFF)[29,30] for PA and PC molecules to account for intermolecular and intramolecular interactions allowing internal relaxations through bond stretching, bond bending, and torsion. We used the Avogradro program[31,32] for a short geometry optimization (conjugate gradient) of previously built molecules. Then, we used antechamber as provided in the AmberTools suite[29,30] to assign final parameters. Partial charges were computed at the ground state using a semi-empirical minimization (conjugate-gradient) approach as provided in Amber sqm version 19. In the aforementioned step, we used the MNDO-type Hamiltonian AM1, a tolerance on the gradient of 0.0005, and we considered that the self-consistent field

method (scf) has converged when the energy difference between two steps is less than 10^{-10} kcal/mol. We also set a system charge of $-3e$ and $+3e$ for PA and PC molecules, respectively, corresponding to the number of monomers carrying the charge for each molecule type (i.e., [2-(methacryloyloxy) ethyl] trimethyl ammonium and acrylic acid for PC and PA molecules, respectively). For systems containing water, we considered the flexible version of the Single Point Charge potential (SPC/Fw) with parameters taken from the work of Wu et al.[33]

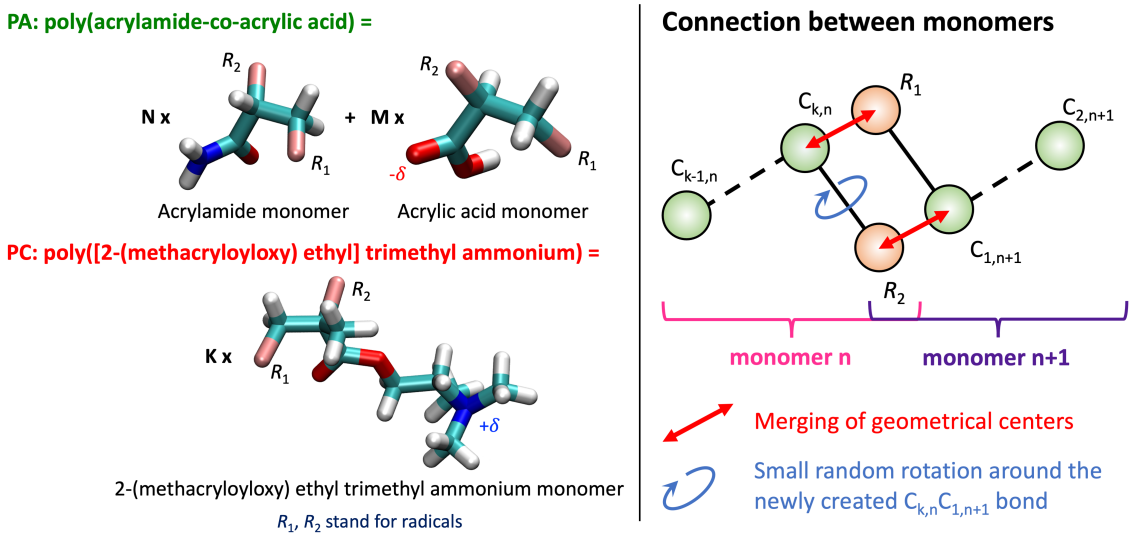

Figure 1: (Left) Snapshots of acrylamide, acrylic acid, and ([2-(methacryloyloxy) ethyl] trimethyl ammonium) monomers and their combination to form poly(acrylamide-co-acrylic acid), i.e., polyanion molecules (or PA), and poly([2-(methacryloyloxy) ethyl] trimethyl ammonium), i.e., polycation molecules (or PC). R_1 and R_2 stand for radicals, where connections between monomers is performed. White-green, blue-green, red-green, green-green, and pink-green licorices stand for bonds between, respectively, a hydrogen atom and a carbon atom, a nitrogen atom and a carbon atom, an oxygen atom and a carbon atom, carbon atoms, and a radical and a carbon atom. N, M, and K stand for the number of acrylamide, acrylic acid, and ([2-(methacryloyloxy) ethyl] trimethyl ammonium) monomers used for the generation of longer polymer chains. δ stand for the partial charge arising from an unsaturated atomic bond. (Right) Sketch of the method we used to connect monomers between them. $C_{k,n}$ stand for a carbon atom belonging to the monomer n and located at the k^{th} position in the carbon chain.

We employed 3 molecular models: pure, bulk water, a neat polyelectrolyte (i.e., pure PC and PA), and an aqueous polyelectrolyte (i.e., a mixture of PC, PA, and water) with PC and PA molecules standing for 20 wt.% of the total mixture. For all models, we started from an

initial cubic simulation box of $10 \times 10 \times 10$ nm^3, where molecules were randomly inserted. We employed 50 ionic pairs of polyions in the pure system and the mixture, meaning that the mole ratio is PC:PA $\sim$ 1:1. Snapshots of initial simulation boxes are shown in Fig. 2. We used 500 and 10515 molecules for pure, bulk water and the mixture, respectively. Initial mass densities (ρ_{m}) were $\sim$0.015, $\sim$0.079, and $\sim$0.393 g/cm^3 for pure, bulk water, neat polyelectrolyte, and the aqueous mixture, respectively.

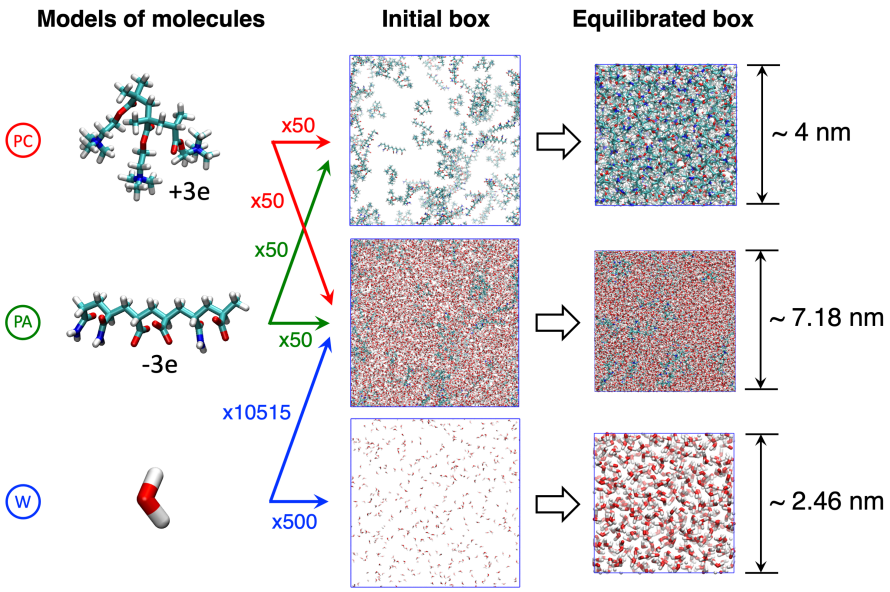

Figure 2: Models of molecules (left), initial simulation boxes (middle), and well-equilibrated simulation boxes (right) of systems considered in this work. White-green, blue-green, red-green, green-green, and red-white licorices stand for bonds between, respectively, a hydrogen atom and a carbon atom, a nitrogen atom and a carbon atom, an oxygen atom and a carbon atom, carbon atoms, and an oxygen atom and a hydrogen atom. PC, PA, and W are symbols that stand for polycation, polyanion, and water, respectively. Numbers stand for the amount of replicas inserted in the initial simulation box.

Using LAMMPS,[34] we performed classical MD to generate well-equilibrated configurations through successive simulations in the canonical ensemble (i.e., the number of atoms (N), the volume (V), and the temperature (T) are constant) and the isothermal-isobaric ensemble (i.e., the number of atoms (N), the pressure (p), and the temperature (T) are constant). Temperature and pressure were maintained in the simulation box using a Nosé-Hoover thermostat[35,36] and a Parinello-Rahman barostat[37] through equations of motion provided by

Shinoda et al.[38] and with relaxation times of 0.1 ps and 1 ps, respectively. We used the P^3M technique[39] to compute Coulomb interactions with a relative error in forces set to 10^{-5}. The cutoff radius for Lennard-Jones and real-space Coulomb interactions was set to $R_{\mathrm{cut}} = 1.2$ nm. Periodic boundary conditions were used in the three directions of space. Apart from specific stages in equilibration processes, we employed a time step of $\delta t = 1$ fs and final equilibration temperature and pressure were set to, respectively, 300 K and 0.101325 MPa. Total simulation times for the relaxation of molecular configurations stand from few tens to few hundreds of ns. Fully relaxed molecular configurations were enclosed in simulation boxes of $2.46 \times 2.46 \times 2.46$ nm^3, $4 \times 4 \times 4$ nm^3, and $7.18 \times 7.18 \times 7.18$ nm^3 corresponding to final mass densities of $\sim$1.007, $\sim$1.23, and $\sim$1.062 g/cm^3 for pure, bulk water, neat polyelectrolyte, and the aqueous mixture, respectively. Snapshots of well-equilibrated molecular configurations are shown in Fig. 2. For the interested reader, full details of equilibration steps are reported in Tab. S1, S2, and S3 of Supporting Information.

We performed additional computations using the NpT ensemble in a temperature range 1-600 K and at a hydrostatic pressure 0.101325 MPa to estimate the glass transition T_{g} of the neat polyelectrolyte through the monitoring of the mass density (ρ_{m}).[40–43] Dynamical effects are not considered allowing only a rough estimation of T_{g}. We used an interval of 50 K between each simulated temperature. The length of each simulation point was 20 ns. Other parameters were the same as above. T_{g} was determined from the crossover of two linear fits in the plot of the specific volume ($V_{\mathrm{sp}} = 1/\rho_{\mathrm{m}}$) as a function of the temperature (see Fig. S1 in Supporting Information). We found $T_{\mathrm{g}} \sim 400$ K, meaning that neat polyelectrolyte has most likely a glassy state at equilibrium.

Steady-shear simulations

No natural systems is precisely adiabatic or isothermal, meaning that a non-equilibrium state produce dissipative heat transferred towards thermal boundaries through radiation, convection, or conduction.[44] However, we can assume a slow heat transfer and a resulting

temperature gradient (transfer process) leading to negligible temperature differences on a microscopic time and length scale.[44] This quasi-isothermal state can be approximated as isothermal at the molecular simulation level.[44] Thus, we investigated the shear viscosity and its related underlying molecular mechanisms by employing Non-Equilibrium Molecular Dynamics (NEMD) combined with the SLLOD algorithm (or homogeneous isothermal shear algorithm)[45–49] as provided in LAMMPS[34] on systems having constant number of molecules, kinetic temperature, volume, and total momentum.[48] It is a widely used and powerful numerical method for the prediction of nano-rheological properties of fluids like viscosity.[47,49–51] In principle, it can be used to calculate linear and non-linear transport coefficients.[44] Even when arbitrarily far from equilibrium, it realistically describes shear flows through the duplication of the transport process occurring in nature[44,51] by imposing a shear rate ($\dot{\gamma}$) to the system.[50] When $\dot{\gamma}$ is applied solely along the x-direction (simple shear), a planar Couette flow is exactly reproduced[44,49] with a streaming velocity ($\vec{u}$) that depends on the location of atoms on the y-axis, i.e., $\vec{u}_i = (\dot{\gamma} y_i, 0, 0)$ for atom i. Monitoring simultaneously the resulting shear stress, the shear viscosity is computed through the constitutive relation:[47–50] $\eta_+(\dot{\gamma}) = -\langle p_{xy} \rangle / \dot{\gamma}$, where p_{xy} stand for the xy-element of the atomic pressure tensor ($\underline{\underline{\mathbf{p}}}$). The aforementioned symmetric second-rank tensor is defined as follows ($p_{xy} = p_{yx}$):[47–49,51,52]

$$p_{yx} = \frac{1}{V} \sum_{i=1}^{N_{\text{atoms}}} \left(m_i \, v_{yi}^{\text{th}} \, v_{xi}^{\text{th}} + y_i F_{xi} \right), \tag{1}$$

with v_{yi}^{th} and v_{xi}^{th} being the y- and x-components of the thermal velocity of atom i, y_i its coordinate on the y-axis, F_{xi} the x-component of the total applied force acting on atom i (i.e., inter- and intra-molecular interactions), and N_{atoms} the total number of atoms in the simulation box. As we employed the atomic formalism for the computation of the xy-element of the pressure tensor, forces are localized on atomic sites.[53] The thermal velocity is determined by subtracting the mean fluid velocity at the atom location $\vec{r}_i$ from the particle velocity,[54] i.e., $\vec{v}_i^{\text{th}} = \vec{v}_i - \vec{u}_i$. As mentioned above, $\vec{u}_i$ is the streaming velocity for a non-

equilibrium steady state.[55] In the SLLOD algorithm, equations of motion are modified with respect to equilibrium MD and given as follows in the atomic formalism:[44,47,49,51]

$$\vec{v}_i = \vec{v}_i^{\,\mathrm{th}} + \vec{u}_i \quad \text{and} \quad \vec{a}_i^{\,\mathrm{th}} = \frac{\vec{F}_i}{m_i} - \vec{n}_x \dot{\gamma} v_{yi}^{\,\mathrm{th}} - \xi \vec{v}_i^{\,\mathrm{th}}, \tag{2}$$

where $\vec{a}_i^{\,\mathrm{th}}$ and m_i stand for the acceleration related to thermal motions and the mass of atom i. $\vec{n}_x$ is a unit vector in the x-direction. ξ is the thermostatting multiplier[44,47,49] for fixing the kinetic energy due to thermal, translational motions. In LAMMPS, we employed the Nosé-Hoover thermostatting approach[35,36,38,49] to ensure that the translational kinetic temperature remains constant.[48,51] In such a way, the thermostat multiplier ξ is obtained by solving the following additional equation of motion:[49,56]

$$\dot{\xi} = \frac{1}{Q}\left[\sum_i^{N_{\mathrm{atoms}}} m_i (\vec{v}_i^{\,\mathrm{th}})^2 - N_{\mathrm{dof}} k_B T_{\mathrm{NH}} \right], \tag{3}$$

where Q stands as an effective mass in the thermostat characterizing the strength of the coupling with the heat bath and acting as an additional degree of freedom to scale atomic, thermal velocities, k_B is Boltzmann's constant, T_{NH} is the target temperature, $N_{\mathrm{dof}} = dN_{\mathrm{atoms}} - N_c$ is the number of internal degrees of freedom, d is the number of system dimensions,[44] and N_c the number of kinetic constraints.[49] For 3-dimensional periodic systems as considered here, we have $d = 3$ and $N_c = 3$, because only the three components of the total momentum are fixed.[49] Instead of Q, it is often more intuitive to use an effective relaxation time $\tau_{\mathrm{NH}} = \sqrt{Q/(N_{\mathrm{dof}} k_B T_{\mathrm{NH}})}$ as damping parameter.[56] This approach of the temperature control called Profile Biased Thermostat (PBT) makes an assumption about the form of the streaming velocity profile (linear).[44] The resulting kinetic temperature is defined as follows:[44]

$$T_{\mathrm{PBT}} = \frac{1}{N_{\mathrm{dof}} k_B} \left\langle \sum_{i=1}^{N_{\mathrm{atoms}}} m_i (\vec{v}_i - \vec{u}_i)^2 \right\rangle = \frac{1}{N_{\mathrm{dof}} k_B} \left\langle \sum_{i=1}^{N_{\mathrm{atoms}}} m_i (\vec{v}_i^{\,\mathrm{th}})^2 \right\rangle, \tag{4}$$

where $\vec{u}_i$ is the "presumed" streaming velocity at the location of atom i.[44]

Equations of motion (Eq. 2) assume a stable, linear profile of streaming velocities ($\vec{u}_i$),[44] which is valid for Reynolds numbers low enough ($Re = (\rho_m \dot{\gamma} L_y^2)/\eta_+$, L_y being the size of the simulation box on the y-axis).[44] For $Re > 10^3$-10^5, the assumption of a linear streaming velocity profile becomes dubious in molecular simulations.[44] Whereas the SLLOD algorithm is correct even at high shear rates, where Reynolds numbers are high and the laminar flow unstable,[44] the PBT thermostat promote simulation artefact like the formation and the stabilization of the string phase (i.e., an alignment of molecules along the flow direction that forms strings) even for simple fluids.[44,51,57] The aforementioned phase is the result of a stabilization process due to the thermostat that assumes a stable, linear velocity profile.[44] Any kink instability in the system leading to fluctuations in the velocity profile is interpreted as heat and the PBT thermostat tries to cool the system down.[44] When the string phase appears, the viscosity drops.[51,58] This simulation artefact can be overcome either with the Profile Unbiased Thermostat (PUT) technique,[44,49] where streaming velocities are computed locally and no assumption is made about the form of the streaming velocity profile, or by using a configurational temperature thermostat.[49,59–61] The interested reader can refer to Supporting Information for more details about the former technique. At low Reynolds numbers (i.e., in a shear-rate range where the string phase was not observed even with the PBT thermostat), computed properties were found indistinguishable between both techniques.[44] Differences appear at high strain rates, but no one has ever observed the string phase while using a PUT thermostat on simple atomic fluids.[44]

Another source of errors due to the thermostat may arise while using the atomic formalism on a molecular system, since the rotational velocity of molecules is not properly taken into account when computing thermal velocities,[62–64] leading to artificially enhanced flows and faster shear-thinning rates. Works pointing out this problem considered rigid or semi-rigid molecules like diatomic chlorine molecules (dumbbell model),[62–64] polymer melts (bead-rod model),[65–67] or polymer molecules in solvent (bead-rod model).[53] Here, we used the all-atom GAFF force field[29,30] that allows internal relaxations within molecules through bond

stretching, bond bending, and torsion. Despite additional degrees of freedom given to atoms belonging to same molecules with respect to rigid or semi-rigid molecular models, high-shear-rate data must be taken with care in our approach due to possible molecular rotations not correctly accounted for.

During shearing, Lees-Edwards sliding brick periodic boundary conditions[48,51,68] ensure that the system is infinite and spatially homogeneous despite discontinuous streaming velocities at boundaries.[44] Movements of particles into and out of the simulation box promote the generation of a stable linear streaming velocity profile with those boundary conditions.[44]

At low strain rates (i.e., in or close to the Newtonian regime), elements of the stress tensor vary widely in the course of the simulation, slowing down the convergence of transport properties like viscosity toward their steady-state values (i.e., it needs longer simulation times).[50] Whereas NEMD is less effective than equilibrium MD with the Green-Kubo approach at low shear rates, NEMD reveals itself orders of magnitude more efficient for large fields.[44] The relative accuracy of NEMD is also much greater than equilibrium MD when increasing the system size.[44] In addition, NEMD simulations allow visualizing and studying underlying molecular mechanisms of transport processes as well as considering the nonlinear response of systems far from equilibrium (e.g., shear dilatancy or shear thinning), which cannot be achieved with equilibrium MD.[44,47,51] Nevertheless, the extrapolation of NEMD viscosities to zero shear rates allows comparing them with viscosities obtained in the frame of the Green-Kubo approach (equilibrium MD).[47,51]

Simulation details

Nano-rheological properties of neat and aqueous polyelectrolytes are characterized through the determination of their viscous behaviors. Molecular scale investigations were performed in a steady-shear mode (see Fig. 3).

In such simulations, a velocity gradient is applied on the y-direction. Velocities on the top of the simulation box (i.e., $v_{\text{top}} = \dot{\gamma} \times L_y$) were taken in the range 10^{-5}-1.2 Å/fs,

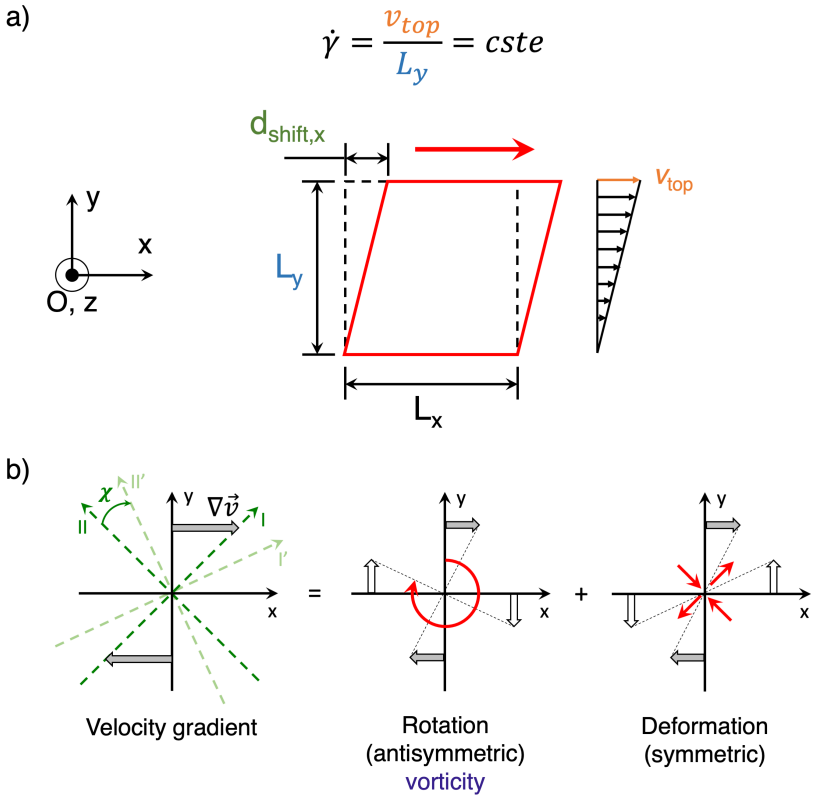

Figure 3: a) Sketch showing details related to steady-shear simulations. b) Decomposition of the velocity gradient into rotational and deformation parts. Green arrows stand for principal axes of the stress tensor (or pressure tensor) in simple shear. χ stand for the rotation of principal axes in nonlinear regimes (i.e., $I \rightarrow I'$ and $II \rightarrow II'$).

which is comparable to experimental values of high-velocity projectiles.[5–8] Whereas we set a time step of $\delta t = 0.25$ fs for velocities $<10^{-3}$ Å/fs, we determined δt in a way that the shift of the simulation box in the xy-plane is constant for each step at higher velocities: $d_{\mathrm{shift,\,x}} = v_{\mathrm{top}} \times \delta t = 2.5 \times 10^{-4}$Å (see Fig. 3). Thus, we ensured the stability of molecular simulations. We used the Ewald sum technique instead of P^{3}M for the computation of Coulomb interactions, but kept the relative error in forces set to 10^{-5}. We employed $\tau_{\mathrm{NH}} =$ 0.1 fs for the Nosé-Hoover thermostat. The cutoff radius for Lennard-Jones and real-space Coulomb interactions was set to $R_{\mathrm{cut}} = 1.2$ nm. Periodic boundary conditions were used in the three directions of space. We considered that the steady state was reached when both the total energy and the shear viscosity exhibited constant values with the simulation time. The lower the shear rate, the longer the required simulation time to reach that state. Results were obtained for total simulation times ($t_{\mathrm{sim.,\,tot}}$) in the range 60 ps-859 ns, 1.22 ps-97 ns, and 2.3 ps-11 ns for pure water, neat polyelectrolyte, and aqueous polyelectrolyte, respectively. Total shearing lengths ($L_{\mathrm{shift,\,x}} = \sum_k l^k_{\mathrm{shift,\,x}}$, with k the k^{th} simulation run and $l_{\mathrm{shift,\,x}} = \sum_i d^i_{\mathrm{shift,\,x}}$, i being the i^{th} step in the k^{th} simulation run) were in the range 102 nm-126 μm, 61 nm-7 μm, and 4.625 nm-1.325 μm, respectively. Whereas longest $t_{\mathrm{sim.,\,tot}}$ were mostly performed at low shear rates, largest $L_{\mathrm{shift,\,x}}$ were performed for high shear rates.

Beyond the shear viscosity η_+ as the straightforward simulation output at constant shear, Hess et al.[69–71] proposed decades ago two additional viscosity coefficients η_- and η_0 accounting for the distortion of the fluid structure. They are computed from spherical components of the atomic pressure tensor, i.e., p_+, p_-, and p_0, which are related to the cartesian components as follows:[52,71]

$$p_+ = p_{xy} = p_{yx}, \;\; p_- = \frac{p_{xx} - p_{yy}}{2}, \;\; \text{and} \;\; p_0 = \frac{p_{zz} - \frac{1}{2}(p_{xx} + p_{yy})}{2}. \tag{5}$$

In a linear flow regime (i.e., Newtonian regime), diagonal, cartesian elements of the atomic pressure tensor are equal to each other and to their equilibrium value meaning that only

p_+ is nonzero and the related shear viscosity is independent of the shear rate.[44,71] Far from equilibrium (i.e., nonlinear flow regimes), this is not true and viscosity coefficients proved themselves useful in characterizing the flow.[44,71] η_0 and η_- are defined as:[44]

$$\eta_0 \equiv -\frac{p_0}{\dot{\gamma}} \text{ and } \eta_- \equiv -\frac{p_-}{\dot{\gamma}}. \tag{6}$$

In nonlinear regimes, η_+, η_-, and η_0 depend on $\dot{\gamma}$.[71] The velocity gradient can be decomposed into rotational and deformation parts (see Fig. 3). Hess[71] showed that η_- is closely associated with the former, whereas η_0 reflects the nonlinear action of the latter. If η_+ is always positive in order to ensure the thermodynamic stability of the system, η_- and η_0 can be either positive or negative.[52,71] η_- is usually positive,[52] but for a vorticity free flow $\eta_- = 0$.[71] η_- and η_0 are related to the more common first and second normal stress coefficients as:[71–73]

$$\Psi_1 = \frac{2\eta_-}{\dot{\gamma}} = \frac{p_{yy} - p_{xx}}{\dot{\gamma}^2} \text{ and } \Psi_2 = -\frac{2\eta_0 + \eta_-}{\dot{\gamma}} = \frac{p_{zz} - p_{yy}}{\dot{\gamma}^2}. \tag{7}$$

Additional viscosity coefficients and normal stress coefficients are difficult to compute accurately, requiring generally both larger and longer simulations in order to achieve an accuracy comparable to the one for shear viscosity.[44,49,53] Evans and Sarman[74] and Menzel et al.[53] showed that those quantities should not be affected by the thermostat as long as the kinetic temperature is not over-constrained. Viscosity coefficients as well as their related normal stress coefficients are useful, since their behavior can be the signature of various interesting macroscopic phenomena like the Weissenberg effect.[44]

In the linear regime of a planar Couette flow, principal axes of the stress tensor (or the pressure tensor) located in the xy-plane are oriented by, respectively, 45° and 135° with respect to cartesian axes.[71] The rotation of those principal axes is also a signature of a non-linear flow and χ provides a quantification of the amount of rotation:[71]

$$\tan 2\chi = \frac{p_-}{p_+} = \frac{\eta_-}{\eta_+}, \tag{8}$$

with $\chi \neq 0$ for a typical nonlinear flow regime.[71] Note that χ is related to the Weissenberg number (Wi_{sh}), which compares the elastic forces to the viscous forces and provides the degree of orientation due to the deformation (anisotropy). Wi_{sh} is defined as follows:[72,75–77]

$$Wi_{\mathrm{sh}} = \frac{p_{xx} - p_{yy}}{p_{xy}} = \frac{2p_-}{p_+} = 2\tan 2\chi \tag{9}$$

for a shear flow along the x-direction and a velocity gradient along the y-direction. O'Sullivan et al.[77] computed Wi_{sh} to determine the validity of the atomic formalism for the pressure tensor, the SLLOD algorithm, and the thermostat (i.e., effects due to rotational velocities). They found values on the order $\sim 10^{-2}$ (domination of viscous forces) as acceptable.[77] They were interested in viscoelasic properties of water using as the main model the rigid SPC/E potential.[77] Computed values for our systems (see Fig. S10 of Supporting Information) lie below 1 at low and intermediate shear rates, the neat polyelectrolyte exhibits highest Wi_{sh} with values very close to 1. Water shows the lowest values ($\sim 10^{-1}$). At high shear rates, Wi_{sh} increases up to 1 or beyond for polyelectrolyte-based systems. Again, despite the employment of a fully flexible force field, high-shear-rate data obtained in the frame of the atomic formalism must be taken with care, since some molecular rotations are possibly not perfectly accounted for.

Finally, we set for each system an upper shear-rate limit ($\dot{\gamma}_{\mathrm{lim}}$) below which we restrained our analysis, since the PBT thermostat and the atomic formalism make data questionable at very high shear rates. For $\dot{\gamma} \geq \dot{\gamma}_{\mathrm{lim}}$, the string phase emerges in the water phase. Snapshots of molecular configurations in Fig. S2 of Supporting Information clearly show the presence of this phase for pure, bulk water beyond $\dot{\gamma}_{\mathrm{lim}}(\mathrm{water}) \sim 1.22 \times 10^{-2}$ fs^{-1}. The drastic drop in the shear viscosity and the net discontinuity in the shear stress shown in Fig. S3 of Supporting Information as well as inhomogeneous potential energy profiles, a long-lasting water structure in pair distribution functions, and high Reynolds numbers (i.e., $Re \sim$ 1000-2500 in the formation zone $1.62 \times 10^{-2} \leq \dot{\gamma} \leq 2 \times 10^{-2}$ and $Re \geq 2500$ for $\dot{\gamma} \geq 2 \times 10^{-2}$ fs^{-1})

in Figs. S4, S7, and S3 of Supporting Information support this conclusion. For the aqueous polyelectrolyte, water domains showing clearly a layering effect are observed for the highest shear rate (see Fig. S2 of Supporting Information), but the drastic drop in shear viscosity and the shear stress discontinuity are not observed (Fig. S3 of Supporting Information). Inhomogeneous potential energy profiles combined with high Reynolds numbers ($Re > 2000$) as shown in Figs. S6 and S3 of Supporting Information support the fact that the string phase is building up for $\dot{\gamma} > 1.25 \times 10^{-2}$ fs^{-1} $= \dot{\gamma}_{\rm lim}$(mixture). As for the aqueous polyelectrolyte, no shear-viscosity drop and shear-stress discontinuities are observed for the neat polyelectrolyte (Fig. S3 of Supporting Information). But, despite relatively low Reynolds numbers ($Re < 85$) and the absence of the string phase, we did observe inhomogeneous potential energy profiles for $\dot{\gamma} > 0.75 \times 10^{-2}$ fs^{-1} $= \dot{\gamma}_{\rm lim}$(neat) (Fig. S5 of Supporting Information). In the remainder of this article, non-physical data located beyond $\dot{\gamma}_{\rm lim}$ were removed.

Results

Shear viscosity

We reported in Fig. 4 shear viscosities computed from NEMD simulations at various shear rates. For pure water, simulation data exhibit a plateau at low $\dot{\gamma}$ (i.e., $1 \rightarrow 2$ on Fig. 4), which is characteristic of a Newtonian behavior. The shear stress is proportional to the shear rate (see Fig. S3 of Supporting Information). In that regime and within standard deviations, we found $\eta_+ \sim 0.85$ cP, which is in good agreement with the experimental value (0.85 cP) and simulation values computed from equilibrium MD trajectories with the Einstein formalism and using the rigid-SPC/E water model (0.82-0.91 cP) reported by Smith and van Gunsteren.[78] In the previous simulation work, the rigid version of the SPC model exhibits viscosities (0.54-0.58 cP) departing strongly from experiments.[78] Flexibility helps to improve performances of the model. Beyond the plateau ($2 \rightarrow 3$), the viscosity starts to decrease when raising the shear rate (shear thinning). The transition between the Newtonian and the

non-Newtonian regime is roughly located at $\dot{\gamma}_{\text{th}} \sim 2 \times 10^{-5}$ fs^{-1}.

The neat polyelectrolyte {PA + PC} exhibits the highest viscosities among the three phases studied in this simulation work and, therefore, the most viscous behavior. We found the shear viscosity decreasing continuously (shear thinning for $1 \rightarrow 2$) down to a minimum ($\sim$1.1 cP) at $\dot{\gamma}_c \sim 2.5 \times 10^{-3}$ fs^{-1} and, then, rising with the shear rate (shear thickening for $2 \rightarrow 3$). No plateau was observed at low $\dot{\gamma}$. The behavior looks like the one of a yield stress fluid characterized by a solid-like behavior below a given yield point and a liquid-like behavior beyond.[79–81] A common signature is the divergence-like trend toward very high values of shear viscosity when approaching the apparent yield stress ($\sigma_{xy,Y}$).[79,80,82] In Fig. S3 of Supporting Information, we reported the shear viscosity plotted as a function of the shear stress σ_{xy} and we did observe the aforementioned behavior when getting close to the apparent yield stress. As a rough estimation of $\sigma_{xy,Y}$, we took the shear stress corresponding to the highest shear viscosity value in the divergence-like part of the curve and found $\sim$269.2 MPa.

For the aqueous polyelectrolyte {PA + PC + water}, the viscosity is a mix between pure water and neat polyelectrolyte. A nearly plateau regime is observed at low shear rates ($1 \rightarrow 2$) with a viscosity close to $\sim$2.1 cP, which is about 2.5 times higher than pure water. Similarly to water, the shear stress is nearly proportional to the shear rate within standard deviations (see Fig. S3 of Supporting Information). The transition between this nearly Newtonian regime and shear thinning is located at a lower shear rate: $\dot{\gamma}_{\text{th}} \sim 5 \times 10^{-6}$ fs^{-1}. In the shear thinning part, viscosity decreases down to $\eta_+ \sim 0.2512$ cP at $\dot{\gamma}_c \sim 5.6 \times 10^{-3}$ fs^{-1}. Beyond that critical point, shear viscosity rises with the shear rate. However, shear thickening is less intense than for neat polyelectrolyte. The higher the concentration in polyelectrolytes, the lower the critical shear rate $\dot{\gamma}_c$ and the more intense the shear thickening, which is a behavior similar to the one observed for colloidal suspensions (i.e., high volume fractions of colloids lessen the critical shear rate and strengthen shear thickening).[4]

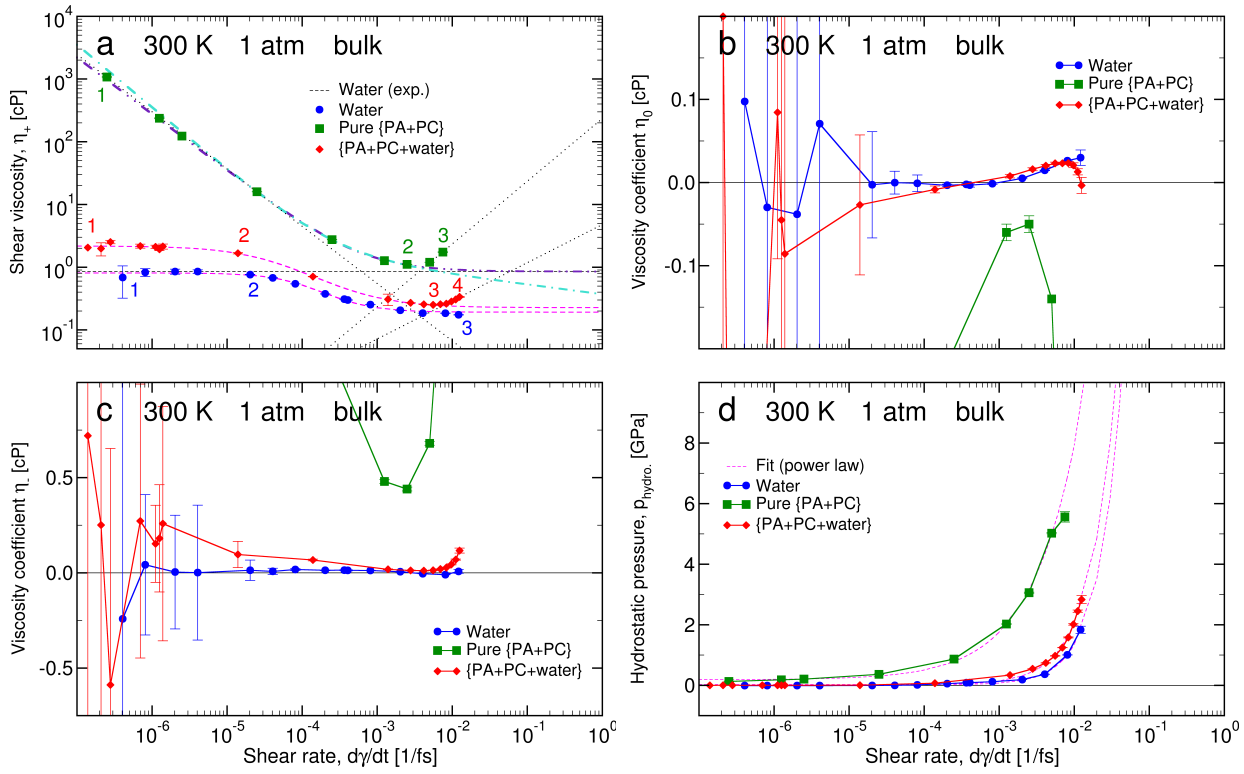

Figure 4: a) Shear viscosities (η_+), b-c) viscosity coefficients η_0 and η_-, and d) hydrostatic pressure ($p_{\text{hydro.}}$) as a function of the shear rate ($\dot{\gamma} = \mathrm{d}\gamma/\mathrm{d}t$) computed for bulk systems at room temperature (300 K) and pressure (1 atm.). Blue filled circles, red filled diamonds, and green filled squares stand for pure water, an aqueous mixture of polycations (PC), polyanions (PA), and water noted {PA+PC+water}, and pure PC and PA noted {PA+PC}. The aqueous mixture has a mole ratio PC:PA $\sim$ 1:1 and PC and PA molecules stand for 20 wt.% of the total mixture. In a), the black dashed line stand for the experimental viscosity of water for same thermodynamics conditions as provided in the work of Smith and van Gunsteren.[78] Pink dashed dotted lines stand for the fit of simulation data with the Cross model.[13,83] The black dotted line, the cyan dashed dotted line, and the indigo dashed-double-dotted line stand for fits of simulation data with the power-law model,[83] the Sisko model,[84] and the Herschel-Bulkley model,[84,85] respectively, for the pure PA and PC system. Colored figures 1, 2, 3, and 4 stand for reference points. In d), pink dashed lines stand for fits of hydrostatic pressures with a power-law model.

Rheological models

In order to further analyze our results, we first introduce the Cross model, which is defined as follows:[13]

$$\eta_+ = \eta_{+,\infty} + \frac{\eta_{+,0} - \eta_{+,\infty}}{1 + (B\dot{\gamma})^{m_{\mathrm{Cr.}}}}, \tag{10}$$

where $\eta_{+,0}$ is the zero-shear viscosity, $\eta_{+,\infty}$ is the infinite-shear viscosity, indicating the viscous behavior of the fluid at high shear rates, $m_{\mathrm{Cr.}}$ is the flow behavior index, and $B = 1/\dot{\gamma}_{\mathrm{th}}$ is the reciprocal of the shear rate determining the onset of shear thinning. This model is well suited for the description of viscosities exhibiting a plateau at low shear rates and a decreasing behavior following a power law at intermediate ones. Neglecting simulation points at high shear rates, we applied the Cross model on data obtained for pure water and the aqueous polyelectrolyte. Results of our fits are shown in Fig. 4. For pure water, we found $\eta_{+,0} \sim 0.8084$ cP, $\eta_{+,\infty} \sim 0.1921$ cP, $B = 9100.98$ fs, and $m_{\mathrm{Cr.}} \sim 1.2928$. The zero-shear viscosity remains consistent with simulation and experimental data with a deviation of 4.9% from the latter. In the shear-rate range considered for the fit, we found absolute errors $\leq$11.07% with respect to simulation values (see Tab. S4 of Supporting Information), showing a relatively good description of the viscosity behavior. A greater absolute error was found for the lowest shear rate (18.15%), but the simulation point exhibits an average value slightly lower than other points at low shear rates and a much larger standard deviation. This is due to the fact that the NEMD technique is less effective than equilibrium ones (e.g., the use of the Green-Kubo formula on trajectories generated with equilibrium MD) in determining the shear viscosity at very low shear rates.[44] From the B parameter of the Cross model, we estimated the onset of shear thinning at $\dot{\gamma}_{\mathrm{th,\,Cr.}} \sim 1.1 \times 10^{-4}$ fs^{-1}, which is an order of magnitude higher than the graphically determined value ($\sim 2 \times 10^{-5}$ fs^{-1}). For the aqueous polyelectrolyte, we found $\eta_{+,0} \sim 2.176$ cP, $\eta_{+,\infty} \sim 0.2266$ cP, $B = 23875.9$ fs, and $m_{\mathrm{Cr.}} \sim 0.9151$. Absolute errors in the shear-rate range considered for the fit were found between 0.16 and 14.34% with respect to simulation values (see Tab. S5 of Supporting

Information). Again, the agreement between the Cross model and simulation data is quite fair. As for pure water, the model fails to predict the onset of shear thinning with $\dot{\gamma}_{\mathrm{th,\,Cr.}} \sim 4.2 \times 10^{-5}$ fs^{-1}, which is also an order of magnitude larger than the graphically determined value ($\sim 5 \times 10^{-6}$ fs^{-1}).

For neat polyelectrolyte, viscosity does not exhibit a plateau at low shear rates. Consequently, the Cross model is not well appropriate for the description of such behavior. Instead, we used the power-law model[83] defined as:

$$\eta_+ = K\dot{\gamma}^{n-1}, \tag{11}$$

where K and n are the consistency and the power-law index, in order to characterize shear thinning ($\dot{\gamma} \leq \dot{\gamma}_c$). In addition, we considered two other models for a better description of data at intermediate shear rates ($2.5 \times 10^{-5} \leq \dot{\gamma} \leq 2.5 \times 10^{-3}$ fs^{-1}), namely, the Sisko model:[84]

$$\eta_+ = \eta_{+,\infty} + K\dot{\gamma}^{n-1}, \tag{12}$$

and the Herschel-Bulkley model:[84,85]

$$\eta_+ = \frac{\sigma_{xy,\,Y}}{\dot{\gamma}} + K\dot{\gamma}^{n-1}, \tag{13}$$

where $\sigma_{xy,\,Y}$ is the yield stress of the fluid. Results from fits of our simulation data were reported in Tab. S6 of Supporting Information. The ability of the three aforementioned models to describe rheological properties of neat polyelectrolyte was assessed by computing the absolute error (see Tab. S7 in Supporting Information). We found that at low shear rates ($<2.5\times10^{-5}$ fs^{-1}) the power-law model describes the best simulated viscosities with absolute errors in the range 0.36-5.67%. The Sisko model underestimates slightly simulation values on average for the whole considered set of data (i.e., $\dot{\gamma} \leq \dot{\gamma}_c$). The larger deviation is observed at the lowest shear rate (10.46%). The Herschel-Bulkley model overestimates more

strongly data at low shear rates (16-31%) and provides a reasonably good agreement with simulation values at intermediate ones (0.02-4.26%) with a description almost as good as the Sisko model (0.02-2.38%). The advantage of the Herschel-Bulkley model is that we can estimate the yield stress of the system at low shear rates: $\sigma_{xy,Y} \sim 351.7$ MPa. Compared with the previous simulation value ($\sim$269.2 MPa), the yield stress from the Herschel-Bulkley model is $\sim$31% higher, which is consistent with the fact that it overestimates simulation values at low $\dot{\gamma}$. The derived yield stress can only be taken as an upper limit. At high shear rates the three models depart strongly from simulation values, which were not taken into consideration in the fitting process. The power-law index n was found lower than 1 for the three models as expected for a shear thinning behavior (see Tab. S6 of Supporting Information).

Finally, we applied the power-law model on viscosity data at high shear rates for polyelectrolyte-based systems with the aim of characterizing more the shear thickening. Results of our fits are reported in Fig. 4. We found $n \sim 2$ and 1.61 and $K \sim 234.4$ and 4.78 for neat and aqueous polyelectrolytes, respectively. The higher consistency and power-law index for the former phase indicate a faster increase of viscosity with $\dot{\gamma}$ during shear thickening and a more viscous phase with respect to aqueous polyelectrolyte, highlighting the well-known solvent properties of water and confirming that the effect of PA and PC concentration on rheological properties is similar to colloidal suspensions.

Viscosity coefficients

We characterized the flow and addressed the distortion of the fluid structure with the shear rate by computing viscosity coefficients η_- and η_0 as well as the hydrostatic pressure, $p_{\text{hydro.}} = \text{trace}\{\underline{\underline{\mathbf{p}}}\}/3$.[69–71] We reported data with error bars computed from those obtained for elements of the pressure tensor in Fig. 4. For pure water and the aqueous polyelectrolyte, η_- and η_0 exhibit large fluctuations as well as very large error bars at low shear rates, $\dot{\gamma} \lesssim 10^{-5}$ fs^{-1} (plateau regime). On the contrary, the neat polyelectrolyte does not show those large

variations in data at low shear rates as can be seen in Fig. S8 a and c of Supporting Information. Apart from the lowest and the highest considered shear rates, error bars are relatively small. In the Newtonian regime (usually at low shear rates), spherical components of the atomic pressure tensor p_- and p_0 as well as η_- and η_0 are expected to vanish, since cartesian, diagonal elements of the atomic pressure tensor are equal to each other and to their equilibrium value. Accurate values of those quantities required both larger and longer simulations to achieve an accuracy comparable to the one for shear viscosity.[44] In this work, simulations were not large enough, especially for water, and not long enough to reach an accuracy comparable to the one we got for the shear viscosity, explaining large variations of our data at low shear rates. Beyond $\dot{\gamma} \sim 10^{-5}$ fs^{-1}, fluctuations cease and error bars become more reasonable allowing a finer analysis of η_- and η_0. Normal stress coefficents and the Weissenberg number are strongly related to η_-, η_0, and χ. The interested reader can find those data in Figs. S9 and S10 of Supporting Information. Again, because of large fluctuations and large error bars, it is difficult to observe a constant behavior of normal stress coefficients at low shear rates that could allow the determination of limiting zero-shear values $\Psi_{1,0}$ and $\Psi_{2,0}$.[66,67,72]

For pure water, the viscosity coefficient η_0 exhibits values close to 0 in the shear-rate range 10^{-5}-10^{-4} fs^{-1} (i.e., $p_{xx} \sim p_{yy} \sim p_{zz}$), corresponding to the onset of shear thinning and where the behavior is nearly Newtonian. Between 10^{-4} fs^{-1} and 10^{-3} fs^{-1}, η_0 takes small negative values (i.e., p_{zz} is slightly greater than $(p_{xx} + p_{yy})/2$) with a local minimum around 5×10^{-4} fs^{-1}. Then, η_0 rises continuously up to $\dot{\gamma} \sim 10^{-2}$ fs^{-1} (i.e., the last portion of shear thinning in viscosity data) and is positive, meaning that $p_{zz} < (p_{xx} + p_{yy})/2$. Looking at the viscosity coefficient η_-, data were close to 0 around 10^{-5} fs^{-1}, meaning that $p_{xx} \sim p_{yy}$. With a close look on η_- beyond 10^{-5} fs^{-1} (see Fig. S8d of Supporting Information), data reveal tiny variations in the shear-rate range 10^{-5}-10^{-2} fs^{-1} with a maximum in positive values (i.e., $p_{xx} < p_{yy}$) at $\dot{\gamma} \sim 5 \times 10^{-4}$ fs^{-1}, corresponding to the local minimum found for η_0, and a minimum in negative values (i.e., $p_{xx} > p_{yy}$) at $\sim 10^{-2}$ fs^{-1} corresponding to the

highest η_0 in the rising portion of data. In order to further characterize the flow in pure water, we reported the parameter χ as a function of the shear rate in Fig. S10 of Supporting Information. $\chi \sim 0$ for shear rates in the range $\sim 5 \times 10^{-6} < \dot{\gamma} \leq 5 \times 10^{-5}$ fs^{-1}, which is characteristic of a Newtonian behavior. Then, χ departs from 0 beyond roughly 5×10^{-5} fs^{-1} depicting the non-linear regime related to shear thinning in the validity limit of the technique ($\dot{\gamma} \leq \dot{\gamma}_{\text{lim}}$). This result confirm the significance of small variations observed in η_0 and η_-.

Looking at the aqueous polyelectrolyte, on the one hand, η_0 increases monotonically up to a maximum at $\dot{\gamma} \sim 10^{-2}$ fs^{-1}, starting from negative values (i.e., $p_{zz} > (p_{xx} + p_{yy})/2$) and ending in positive ones (i.e., $p_{zz} < (p_{xx} + p_{yy})/2$). Once the maximum is reached, η_0 rapidly drops to negative values. On the other hand, η_- is always positive beyond $\dot{\gamma} \sim 10^{-5}$ fs^{-1} (i.e., $p_{xx} < p_{yy}$), but decreases down to a minimum at $\dot{\gamma} \sim 10^{-2}$ fs^{-1} before rising at higher shear rates. Focusing on the parameter χ shown in Fig. S10 of Supporting Information, we observed net positive values for $\dot{\gamma} \geq 10^{-6}$ fs^{-1}, where we observed less variations of η_0 and η_- with more reasonable error bars. In fact, χ for the aqueous polyelectrolyte shows that, even if close, the fluid mixture is not fully Newtonian at low $\dot{\gamma}$.

For the neat polyelectrolyte, whereas η_0 is always negative (i.e., $p_{zz} > (p_{xx} + p_{yy})/2$), η_- remains in positive values (i.e., $p_{xx} < p_{yy}$). From low to high shear rates, η_0 increases up to a maximum ($\dot{\gamma} \sim 2 \times 10^{-2}$ fs^{-1}) and decreases beyond. Similarly, η_- lessens down to a minimum located at the same shear rate as for the maximum in η_0 prior to rise for larger $\dot{\gamma}$. The parameter χ shows the highest values ($\gtrsim$0.2) among the three studied systems, depicting its strong non-Newtonian behavior (see Fig. S4 of Supporting Information). Interestingly, Rainwater, Hanley et al.[52,86] provided conditions at which the Weissenberg effect occurs (i.e., the fluid climbs the inner cylinder of an experimental device having a central spinning rod): $\eta_0 < 0$, $\eta_- > 0$, and $|\eta_0| > 0.25\,\eta_-$. From the ratio $|\eta_0|/\eta_-$ and given the fact that the first two conditions are met in our results on the whole range of investigated shear rates, simulations predict a Weissenberg effect for $\dot{\gamma} \gtrsim 5 \times 10^{-3}$ fs^{-1}. It corresponds to the shear

thickening part in the rheogram. In addition, we found for the lowest shear rate ($\sim 2.5 \times 10^{-7}$ fs^{-1}) a ratio $|\eta_0|/\eta_- \sim 0.25$, which is close to the fulfillment of the three required conditions. Further investigations are needed to conclude on wether or not the Weissenberg effect may occur at low $\dot{\gamma}$. For clarity, only small portions of η_0 and η_- curves are shown in Fig. 4. The interested reader can find the whole curves in Fig. S8 of Supporting Information.

Finally, hydrostatic pressures depict similar behavior at low and intermediate shear rates for pure water, the aqueous polyelectrolyte, and the neat polyelectrolyte. $p_{\mathrm{hydro.}}$ rises continuously with the shear rate. Hydrostatic pressures were the highest for the neat polyelectrolyte, then, came the aqueous mixture and the pure water phase. Rainwater, Hanley et al.[52] previously found a power-law dependance of the hydrostatic pressure for soft spheres, namely, $p_{\mathrm{hydro.}} = p^{(0)} + p^{(1)}\dot{\gamma}^{n_{\mathrm{h}}}$ with $n_{\mathrm{h}} = 3/2$ and $p^{(0)}$ the equilibrium pressure at the given temperature and density. We applied with success the aforementioned model to our data at low and intermediate shear rates without constraining the exponent n_{h}. Fitting parameters $p^{(0)}$, $p^{(1)}$, and n_{h} were reported in Tab. S8 of Supporting Information. For all phases, we found $n_{\mathrm{h}} < 3/2$ and the higher the water content ($x_{\mathrm{wc.}}$ [wt.%]), the closer to 3/2. Thus, n_{h} varies oppositely with the mass density (ρ_{m}), which is controlled by the water content, and follows the linear relationship: $n_{\mathrm{h}}(x_{\mathrm{wc.}}) = 0.0069 \cdot x_{\mathrm{wc.}} + 0.6914$. This conclusion is in line with previous works that showed that the exponent is a simple linear function of the temperature (T) and the mass density of the system:[49] $n_{\mathrm{h}} = C_1 + C_2 T - C_3 \rho_{\mathrm{m}}$, with C_1, C_2, and C_3 three constants. The temperature is also constant in our work. On the contrary, $p^{(0)}$ and $p^{(1)}$ deviate from a linear behavior with $x_{\mathrm{wc.}}$ and seems to exhibit some curvature. However, in this study, we only have a 3-point data set, making spurious the use of quadratic polynomial forms for the fit of data: there is as much degrees of freedom as data points. Further investigations are needed with more intermediate simulation points to confirm this trend.

Energy

With the aim of better understanding underlying mechanism for shear thinning and shear thickening in our systems, we investigated potential energy contributions. We omitted the kinetic energy, since it does not show significant variations as a function of $\dot{\gamma}$; the system temperature is kept relatively constant with the PBT thermostat. We independently monitored the van der Waals pairwise energy (vdw), Coulomb interactions in the real space (coul.) and the reciprocal one (long), and the intramolecular energy (mol.) including bond stretching, angle bending, and torsion. Mainly, van der Waals and Coulomb contributions refer to intermolecular interactions, even if with the all-atom GAFF force field non-bonded interactions are allowed among sufficiently separated atoms of the same molecule (i.e., beyond the third consecutive bonded atoms). We reported those contributions to the potential energy in Fig. 5.

Similarly to the hydrostatic pressure, the total, potential energy exhibits the same general behavior for the three systems: whereas it increases smoothly at low shear rates, it rises sharply for the highest ones. The faster rise of potential energy corresponds to shear thickening in rheograms for polyelectrolyte-based systems and can be seen as a signature of this rheological phenomenon. As for the hydrostatic pressure, the potential energy behavior mostly follows a power-law model:[49] $U = U_0 + U_1\dot{\gamma}^{n_\mathrm{h}}$, with U_0 and U_1 fitting parameters. We applied the aforementioned model on our data and used the same exponents as those found for hydrostatic pressures, since thermodynamic conditions are the same. We reported fitting results in Tab. S8 of Supporting Information. Whereas total, potential energies roughly follow a power law at low and intermediate shear rates, simulation data of polyelectrolyte-based systems depart from the model for $\dot{\gamma} \gtrsim 10^{-2}$ fs^{-1}, where shear thickening occurs.

Looking at the different contributions to the potential energy, we found that whereas the raise originates from van der Waals interactions and Coulomb interactions in the real space (short-range) for pure water, it originates mostly from intramolecular interactions and van der Waals interactions for neat and aqueous polyelectrolytes. The difference with pure

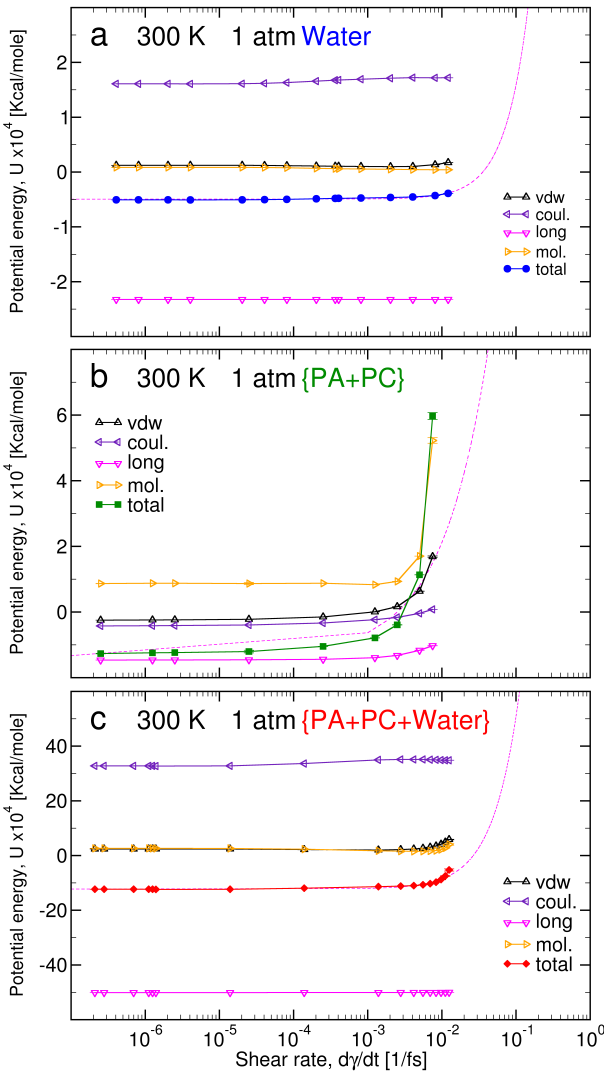

Figure 5: Different contributions to the potential energy as a function of the shear rate ($\dot{\gamma} = \mathrm{d}\gamma/\mathrm{d}t$) for a) pure water, b) pure polycations (PC) and polyanions (PA), and c) an aqueous mixture of PC, PA, and water with a mole ratio PC:PA $\sim$ 1:1 and PC and PA molecules standing for 20 wt.% of the total mixture. In addition to the total, potential energy (total), we reported contributions related to van der Waals pairwise interactions (vdw), Coulomb interactions in the real space (coul.) and the reciprocal one (long), and the intramolecular energy (mol.) including bond stretching, angle bending, and torsion. Pink dashed lines stand for fits of total, potential energies with a power-law model.

water can be simply explained by the presence of PA and PC ions that are larger than water molecules, i.e., with more internal relaxation modes. When $\dot{\gamma}$ increases, there is a competition between the rate at which the simulation box is sheared (i.e., the frequency of deformation) and relaxation modes of PA and PC molecules through bond stretching, angle bending, and torsion. Bond stretching modes often exhibit the highest frequencies. Therefore, from stiffness constants (K_{h}) provided by the all-atom GAFF force field that describes covalent bonds as harmonic oscillators (i.e., oscillation frequencies are defined as $f_i = (1/2\pi)\sqrt{K_{i,\mathrm{h}}/M_i}$ with M_i the molar mass of atom i), we computed the frequency range where relaxation occurs for PA and PC molecules. We found values between $\sim 3 \times 10^{-6}$ and $\sim 2 \times 10^{-5}$ fs^{-1}, which is about 2-3 orders of magnitude lower than where dilatancy occurs. The lack of internal relaxation in PA and PC molecules contribute to dilatancy or the increase of potential energy. Another source is the increasing difficulty for the fluid to locally rearrange as depicted by the rise in van der Waals interactions.

Structure

In addition to the analysis of the potential energy, we analyzed the molecular structure of our systems as a function of the shear rate. We considered first radial distribution functions of molecule centers of mass ($g(r)$) that measure radial variations of the local density with respect to the mean, bulk density: $g(r) = \rho_{\mathrm{loc.}}(r)/\rho_{\mathrm{bulk}}$. This quantity is very useful, since it can be related to structure factors obtained from X-ray experiments,[87] for example. We reported simulation results in Fig. 6.

For water, the molecular structure in the Newtonian regime ($1 \rightarrow 2$) is barely affected by the shear rate and exhibits features of the equilibrium structure with a large, first peak around 0.28 nm, giving the average distance between nearest neighbor molecules, followed by two less intense peaks around 0.46 and 0.68 nm, corresponding to molecules in second and third hydration shells, respectively. Beyond the third peak, $g(r)$ is roughly constant and equals 1. Such behavior is typical of a liquid.[87] Then, shear thinning ($2 \rightarrow 3$) results in a

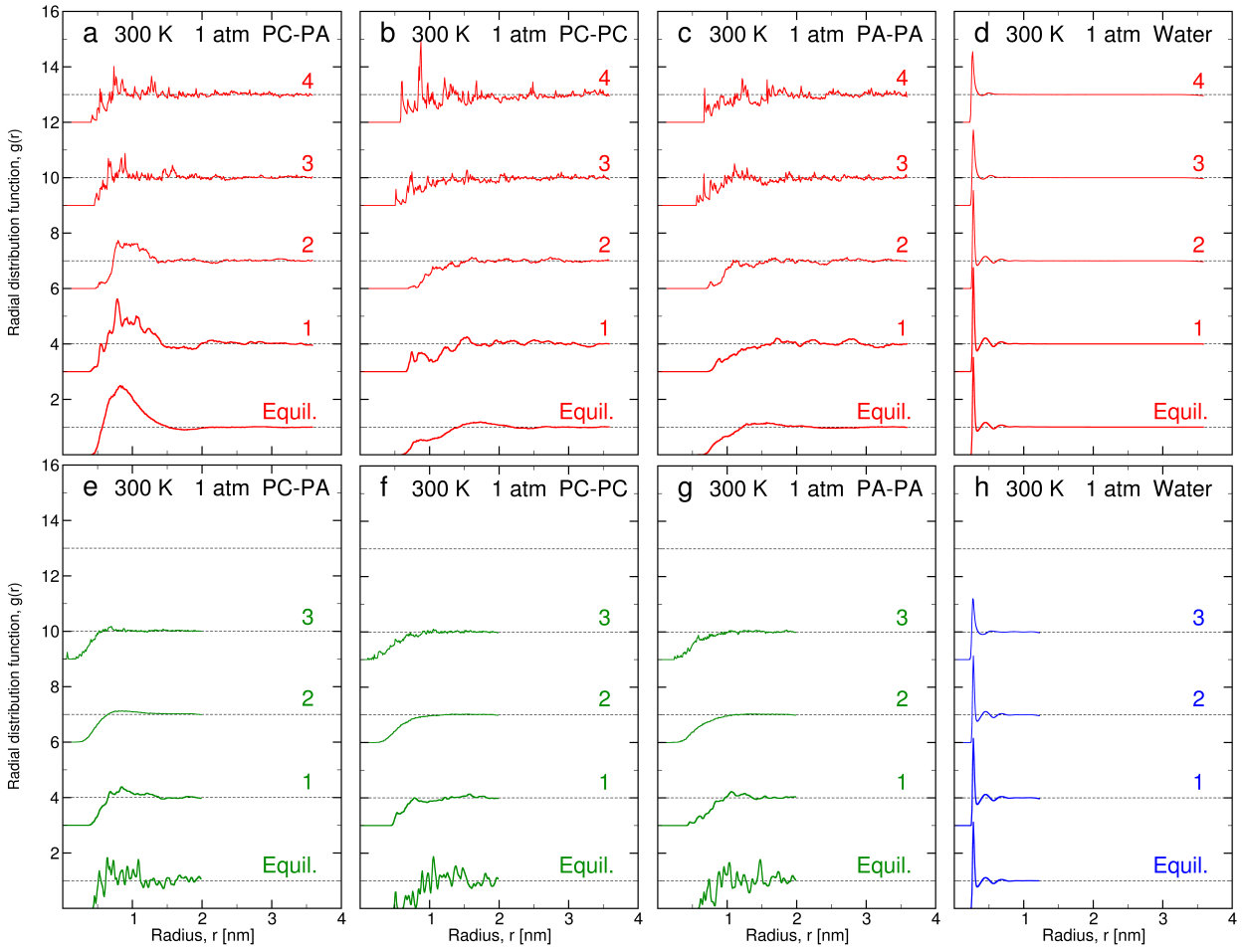

Figure 6: Radial distribution functions ($g(r)$) for the mixture of polycations (PC), polyanions (PA), and water with a mole ratio PC:PA $\sim$ 1:1 and PC and PA molecules standing for 20 wt.% of the total mixture (red solid lines in a-d), pure PA and PC (green solid lines in e-f), and pure water (blue solid lines in h). Colored figures refer to simulation conditions labelled in Fig. 4. Red figures 1, 2, 3, and 4 stand for, respectively, $\dot{\gamma} \sim 1.39 \times 10^{-7}$, 1.39×10^{-5}, 6.97×10^{-3}, and 1.25×10^{-2} fs^{-1}. Green figures 1, 2, and 3 stand for, respectively, $\dot{\gamma} \sim 2.5\times10^{-7}$, 2.5×10^{-3}, and 0.75×10^{-2} fs^{-1}. Blue figures 1, 2, and 3 stand for, respectively, $\dot{\gamma} \sim 4.06 \times 10^{-7}$, 2.03×10^{-5}, and 1.21×10^{-2} fs^{-1}. Data computed at equilibrium (Equil.) with no applied shear were reported as a reference. Dashed dotted lines stand for the bulk density value.

disruption of second and third hydration shells and a reduction of the first peak intensity. This can be related to the hydrogen bond network that is disrupted to facilitate the flow.

Looking at data for the aqueous polyelectrolyte, we observed similarly a water structure that is slightly affected by the shear rate in the Newtonian regime ($1 \rightarrow 2$) with three distinct peaks at roughly 0.28, 0.45, and 0.68 nm. At the end of shear thinning (3), the first peak is still located at $\sim$0.28 nm, but less intense, the second peak is slightly shifted toward larger distances ($\sim$0.52 nm), and the third peak has fully disappeared. At the highest shear rate (4), where dilatancy has occurred, the third peak has still vanished, whereas the first peak (resp. the second peak) is slightly shifted toward a lower (resp. higher) value, $\sim$0.26 nm (resp. $\sim$0.54 nm). Focusing on the structure of ions in water, we observed an equilibrium distance between pairs of PA and PC ions of roughly 0.83 nm. When comparing with $g(r)$ between PC pairs and PA pairs, the aforementioned peak occurs at the shortest distance with the highest intensity, meaning ion pairing in our equilibrated mixture. Applying a shear rate, but remaining in the Newtonian regime, the first peak is slightly shifted toward a lower value $\sim$0.8 nm and reduces in intensity with the rise of $\dot{\gamma}$. Upon shear thinning ($2 \rightarrow 3$), $g(r)$ becomes noisier and noisier and the well-defined peak related to ionic pairs vanishes. Data points fluctuate around the bulk density value ($g(r) \sim 1$), meaning that the local ionic structure in water is strongly disrupted. During shear thickening ($3 \rightarrow 4$), data for all pair distribution functions of polyions exhibit similar profiles with a noisy behavior at short intermolecular distances and a rapid convergence to 1 at longer range.

In the case of neat polyelectrolyte, radial distribution functions computed from equilibrium trajectories (equilibrium MD) exhibit peaks at short, but also longer range reflecting a structured system. Comparing $g(r)$ data between same molecule pairs (PC-PC and PA-PA) with those generated between PC and PA molecules, we observed that the first, intense peak arises for pairs of PC and PA, meaning that first nearest neighbors are of the opposite charge, which suggests a fluid structure most likely due to ion pairing in a similar way as what can be seen in ionic liquids with Coulomb ordering.[88] Ion pairing is enhanced in our

study because we considered small PA and PC molecules that contain only few monomers leading to spatially concentrated charges in the molecular backbone. It does not fully correspond to experiments,[19,20] where charge carrying monomers of PA molecules are diluted with more neutral units (i.e., acrylamide monomers). Therefore, the neat polyelectrolyte is most likely in a glassy state rather than a liquid one at equilibrium, which is corroborated by high viscosities and a simulation temperature (300 K) being under the estimated $T_g \sim 400$ K. In the shear thinning part of the rheogram ($1 \rightarrow 2$), computed radial distribution functions smoothen and finally exhibit a more liquid-like behavior at the minimum shear viscosity (i.e., 2 in Fig. 6). The local structure of the aforementioned liquid is slight with only a broad peak around 0.8 nm in $g(r)$ between PA and PC molecules. During shear thickening ($2 \rightarrow 3$), pair distributions exhibit similar profiles, but get slightly noisier when increasing the shear rate.

Finally, the aqueous polyelectrolyte with a mole ratio PC:PA $\sim$ 1:1 and where PC and PA molecules stand for 20 wt.% of the total mixture could be assimilated to a colloidal suspension. In such systems, shear thickening may occur through the formation of hydroclusters.[2,4] Using a cluster-size-analysis method similar to the ones employed by Headen et al.[89] for the study of asphaltene aggregation or Mustan et al.[90] for the study of aggregation patterns in aqueous solutions of bile salts, we investigated the size (N_{clusters}) and the number (n_{clusters}) of clusters in the mixture and how they behave with the shear rate. Our approach is solely based on a geometrical criterium, i.e., when the k$^{\text{th}}$ atom $a_{k,i}$ belonging to molecule i is located within a maximum radial distance (R_{clusters}) from the q$^{\text{th}}$ atom $a_{q,j}$ of molecule j, we considered molecules i and j as aggregated (see Fig. 7). Note that in some approaches like the one of Totton et al.[91] for the study of polycyclic-aromatic-hydrocarbon clustering a time-length criterium is used to determine if two adjacent molecules are clustered. A time-based analysis is useful in order to discriminate between collisions of molecules resulting in sticking and those that do not. As a first approximation, we neglected this effect. Furthermore, the choice of the maximum radial distance R_{clusters} is usually arbitrary and can significantly affect results.[91] In some cases, R_{clusters} is determined from minimum distance

distributions.[90] Here, we chose $R_{\text{clusters}} \sim 0.35$ nm, corresponding roughly to the upper range of energy-minimum locations in non-bonding, pair interactions among atoms of the all-atom GAFF force field (0.12-0.382 nm for Lennard-Jones potentials).

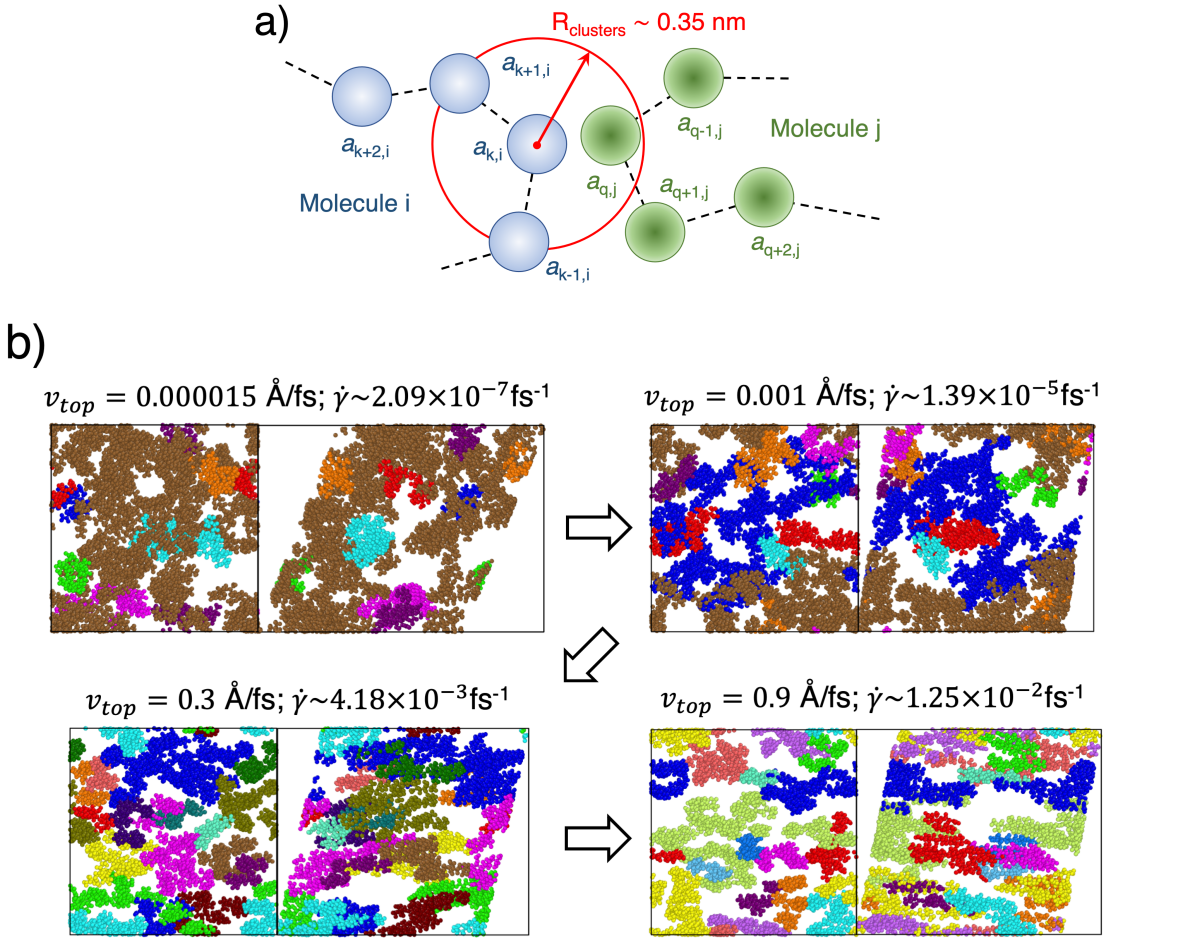

Figure 7: a) Sketch showing the geometrical criterium used to consider two molecules i and j as aggregated; b) snapshot of molecular configurations for the mixture of polycations (PC), polyanions (PA), and water with a mole ratio PC:PA $\sim$ 1:1 and PC and PA molecules standing for 20 wt.% of the total mixture. Snapshots show clusters of ions at various shear rates: $\dot{\gamma} \sim 2.09 \times 10^{-7}$, 1.39×10^{-5}, 4.18×10^{-3}, and 1.25×10^{-2} fs^{-1}. Water molecules were removed for clarity. A different color was assigned for each clusters. Colors were arbitrarily given to clusters for each shear rate.

Using the OVITO program,[92] we generated snapshots of molecular configurations showing clusters of ions at various shear rates and reported them in Fig. 7. We arbitrarily attributed a color for each cluster in the simulation box without keeping consistency between snapshots taken at different shear rates. The aim is to show how the size and the number of clusters

evolve with $\dot{\gamma}$. The more the number of colors, the more the number of clusters. Raising the shear rate, snapshots qualitatively show that there is more clusters (i.e., more colors) with smaller sizes (i.e., colors occupy less space in the simulation box). In particular, we do not observed a sudden increase of cluster sizes at the onset of shear thickening. In order to quantify what is observed in snapshots, we directly computed the size (N_{clusters}) and the number (n_{clusters}) of clusters and reported data in Fig. 8.

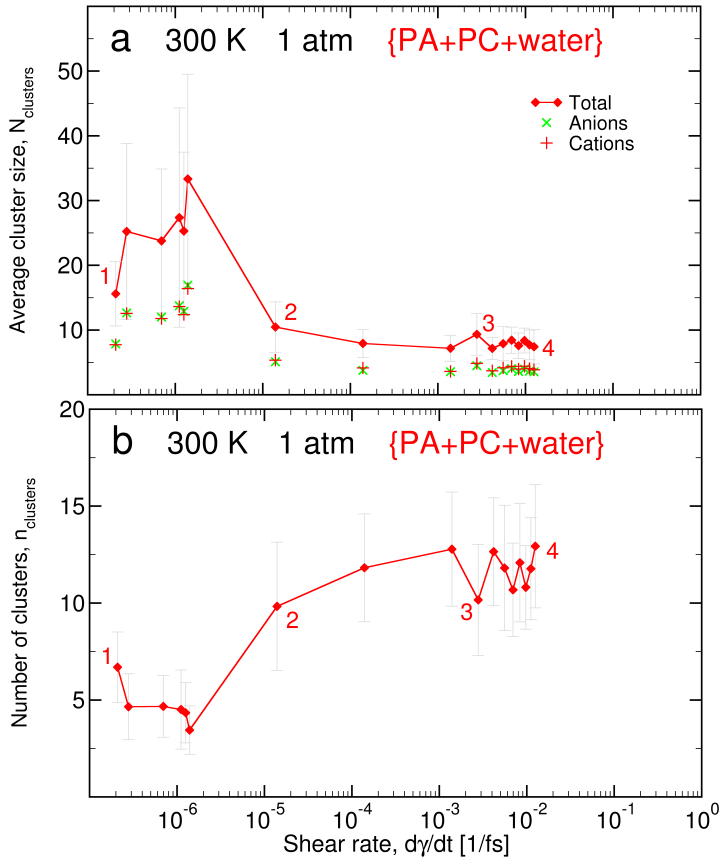

Figure 8: a) Average cluster size (N_{clusters}) and b) number of clusters (n_{clusters}) in the simulation box as a function of the shear rate for the mixture of polycations (PC), polyanions (PA), and water with a mole ratio PC:PA $\sim$ 1:1 and PC and PA molecules standing for 20 wt.% of the total mixture. Red plusses and green crosses stand for the average amount of, respectively, cations and anions in clusters (i.e., the chemical composition of clusters). Standard deviations were shown in light grey.

For the average cluster size, we observed biggest aggregates of ionic species in the nearly Newtonian regime ($1 \rightarrow 2$) with a number of involved molecules in the range 15-35. Then,

N_{clusters} slightly decreases during shear thinning ($2 \rightarrow 3$) and reaches a nearly constant value ($\sim$8.4) given standard deviations when shear thickening occurs. So, increasing the shear rate results mainly in a decrease of cluster sizes. Looking at the chemical composition of clusters found in the simulation box, we observed that the mole ratio of the whole simulation box (PC:PA $\sim$ 1:1) is respected on average. In addition to the size of clusters, we also monitored their average number in the simulation box. In the nearly Newtonian regime, n_{clusters} exhibits the lowest values ($\sim$4.5). Then, the number of clusters increases from the onset of shear thinning to the onset of shear thickening. From 3 to 4, the average number of clusters is nearly constant ($\sim$11.5). Therefore, N_{clusters} and n_{clusters} computed at various shear rates confirmed what was qualitatively observed in snapshots of molecular configurations, i.e., raising $\dot{\gamma}$ implies more clusters with smaller sizes.

Summary and outlook

We employed non-equilibrium molecular dynamics to provide a clearer understanding of molecular mechanisms underlying non-Newtonian behaviors of neat and aqueous polyelectrolytes at intermediate and high shear rates. These mechanisms are relevant to our ongoing efforts in developing smart, structural materials manufactured with water-based shear thickening fluids that resist external mechanical stimuli like impacts. We designed three molecular models including pure water, neat polyelectrolyte, and an aqueous mixture with polycations (PC) and polyanions (PA) being poly([2-(methacryloyloxy) ethyl] trimethyl ammonium) and poly(acrylamide-co-acrylic acid), respectively. As a first step, we employed short PC and PA molecules, where charges are highly concentrated in the polymer chain, at a 1:1 mole ratio.

From steady-shear simulations, we monitored the viscosity of those three systems. Whereas neat polyelectrolyte does not exhibit a plateau (non-Newtonian behavior) at low shear rates similarly to yield-stress fluids, pure water and the aqueous polyelectrolyte do have one. From viscosity coefficients, we showed that pure water in that regime has a fully Newtonian be-

havior. For the aqueous polyelectrolyte, viscosity coefficients exhibit a behavior departing slightly from a Newtonian one. At high shear rates, polyelectrolyte-based systems showed shear thickening. All systems experienced shear thinning at intermediate shear rates. Using the Cross model, we successfully described data at low and intermediate $\dot{\gamma}$ for pure water and the aqueous polyelectrolyte. However, the model was unable to predict accurately the transition between the Newtonian regime and shear thinning with an overestimation by about one order of magnitude. Whereas the power-law model described the best viscosity data at low shear rates for the neat polyelectrolyte, Sisko and Herschel-Bulkley models proved better at intermediate ones. The latter model allows estimating the yield stress ($\sim$351.7 MPa), but, since it overestimates data at low shear rates, it was found $\sim$31% higher than the simulation value ($\sim$269.2 MPa). Viscosities of polyelectrolyte-based systems roughly follow a power law during shear thickening.

To elucidate mechanisms at the origin of shear thinning and thickening, we first investigated different contributions in potential energy data. We found the same general, power-law behavior for the three systems. Whereas the energy rise is driven by pair interactions including van der Waals and Coulomb ones for pure water at high shear rates, intramolecular contributions, including bond stretching, angle bending, and torsion, and van der Waals interactions are the main contributions to the faster energy increase for polyelectrolyte-based systems. This rise of the potential energy at high shear rates was attributed to the increasing difficultly of our systems to relax upon shear. It results in an increase of intermolecular interactions for small molecules like water and intramolecular interactions for larger molecules like polyelectrolytes.

Then, we analyzed molecular structures by considering first radial distribution functions between centers of mass of molecules. For water and aqueous polyelectrolyte, the structure is not or barely affected by the shear rate in the Newtonian or near Newtonian regime. Then, the structure starts to disrupt during shear thinning with a reduction of the local structure for water as well as ion pairing. For the latter, the first peak in the pair distribution

function between polycations and polyanions weakens. Shear thinning affects the structure of neat polyelectrolyte with $g(r)$ that smoothens. When shear thickening occurs, the local ionic structure vanishes for polyelectrolyte-based systems. Finally, we employed cluster size analysis to study cluster properties as a function of $\dot{\gamma}$ in the aqueous polyelectrolyte. Results showed that raising $\dot{\gamma}$ yields more clusters with smaller sizes.

This method and findings underscore the importance of accounting for the molecular nature of polyelectrolytes (or polyion complex) to investigate their nano-rheological properties and set the basis for considering mixtures closer to experimental ones with longer polymer chains (higher molecular weights) and a mole ratio PC : PA $\sim 1 : 4$.

Acknowledgement

This work was supported by Innovative Science and Technology Initiative for Security Grant Number JPJ004596, ATLA, Japan. The authors acknowledge the Center for Computational Sciences of the University of Tsukuba and the AI Bridging Cloud Infrastructure of the National Institute of Advanced Industrial Science and Technology (AIST) for providing computational resources.

Supporting Information Available

Supporting Information includes computational methods, snapshots of molecular configurations, details on fits with rheological models, normal stress coefficients, potential energy profiles, and Weissenberg numbers.

References

(1) Ding, J.; Li, W.; Shen, S. Z. Research and Applications of Shear Thickening Fluids. *Recent Patents on Materials Science* **2011**, *4*, 43–49.

(2) Pinto, F.; Meo, M. Design and Manufacturing of a Novel Shear Thickening Fluid Composite (STFC) with Enhanced out-of-Plane Properties and Damage Suppression. *Applied Composite Materials* **2017**, *24*, 643–660.

(3) Nesrinne, S.; Djamel, A. Synthesis, characterization and rheological behavior of pH sensitive poly(acrylamide-co-acrylic acid) hydrogels. *Arabian Journal of Chemistry* **2017**, *10*, 539–547.

(4) Zarei, M.; Aalaie, J. Application of shear thickening fluids in material development. *Journal of Materials Research and Technology* **2020**, *9*, 10411–10433.

(5) Savvateev, A. F.; Budin, A. V.; Kolikov, V. A.; Rutberg, P. G. High-Speed Penetration Into Sand. *International Journal of Impact Engineering* **2001**, *26*, 675–681.

(6) Smirnov, N. N.; Kiselev, A. B.; Nikitin, V. F. High-speed collisions of space debris particles with gas-filled shells. *Vestnik Moskov. Univ. Ser. 1. Mat. Mekh.* **2003**, *1*, 54–66.

(7) Soulard, R.; Quinn, M. N.; Tajima, T.; Mourou, G. ICAN: A novel laser architecture for space debris removal. *Acta Astronautica* **2014**, *105*, 192–200.

(8) Smirnov, N. N.; Kiselev, A. B.; Smirnova, M. N.; Nikitin, V. F. Space traffic hazards from orbital debris mitigation strategies. *Acta Astronautica* **2015**, *109*, 144–152.

(9) Smith, M. I.; Besseling, R.; Cates, M. E.; Bertola, V. Dilatancy in the flow and fracture of stretched colloidal suspensions. *Nature Communications* **2010**, *1*, 114.

(10) Brown, E.; Forman, N. A.; Orellana, C. S.; Zhang, H.; Maynor, B. W.; Betts, D. E.; DeSimone, J. M.; Jaeger, H. M. Generality of shear thickening in dense suspensions. *Nature Materials* **2010**, *9*, 220–224.

(11) Eliassaf, J.; Silberberg, A.; Katchalsky, A. Negative thixotropy of aqueous solutions of polymethacrylic acid. *Nature* **1955**, *176*, 1119.

(12) Hill, A.; Candau, F.; Selb, J. Properties of Hydrophobically Associating Polyacrylamides: Influence of the Method of Synthesis. *Macromolecules* **1993**, *26*, 4521–4532.

(13) Mrokowska, M. M.; Krztoń-Maziopa, A. Viscoelastic and shear-thinning effects of aqueous exopolymer solution on disk and sphere settling. *Scientific Reports* **2019**, *9*, 7897.

(14) Bokias, G.; Hourdet, D.; Iliopoulos, I. Positively charged amphiphilic polymers based on poly(N-isopropylacrylamide): Phase behavior and shear-induced thickening in aqueous solution. *Macromolecules* **2000**, *33*, 2929–2935.

(15) Chang, Y.; McCormick, C. L. Water-soluble copolymers: 57. Amphiphilic cyclocopolymers of diallylalkoxybenzyl-methylammonium chloride and diallyl-dimethylammonium chloride. *Polymer* **1994**, *35*, 3503–3512.

(16) Basu, S.; Vutukuri, D. R.; Shyamroy, S.; Sandanaraj, B. S.; Thayumanavan, S. Invertible amphiphilic homopolymers. *Journal of the American Chemical Society* **2004**, *126*, 9890–9891.

(17) Maerker, J. M.; Sinton, S. W. Rheology Resulting from Shear-Induced Structure in Associating Polymer Solutions. *Journal of Rheology* **1986**, *30*, 77–99.

(18) Lele, A.; Shedge, A.; Badiger, M.; Wadgaonkar, P.; Chassieux, C. Abrupt shear thickening of aqueous solutions of hydrophobically modified poly (N,N'-dimethylacrylamide-co-acrylic acid). *Macromolecules* **2010**, *43*, 10055–10063.

(19) Takeda, R.; Tsurusaki, K.; Honda, G.; Wakatsuki, S. Study on Dilatant Properties of Aqueous Ionic Polymer Solution. *Research Report of Kanagawa Prefectural Industrial Technology Center* **2011**, 22–26.

(20) Takeda, R.; Tsurusaki, K.; Honda, G. Study on Dilatant Properties of Aqueous Ionic Polymer Solution (2). *Research Report of Kanagawa Prefectural Industrial Technology Center* **2012**, *18*, 14–18.

(21) Sun, G.; Zhang, M.; He, J.; Ni, P. Synthesis of amphiphilic cationic copolymers poly[2-(methacryloyloxy)ethyl trimethylammonium chloride-co-stearyl methacrylate] and their self-assembly behavior in water and water-ethanol mixtures. *Journal of Polymer Science: Part A: Polymer Chemistry* **2009**, *47*, 4670–4684.

(22) McCormick, C. L.; Middleton, J. C.; Cummins, D. F. Water-Soluble Copolymers. 37. Synthesis and Characterization of Responsive Hydrophobically-Modified Polyelectrolytes. *Macromolecules* **1992**, *25*, 1201–1206.

(23) Biggs, S.; Selb, J.; Candau, F. Copolymers of acrylamide N-alkylacrylamide in aqueous solution: the effects of hydrolysis on hydrophobic interactions. *Polymer* **1993**, *34*, 580–591.

(24) Krieg, A.; Pietsch, C.; Baumgaertel, A.; Hager, M. D.; Remzi Becer, C.; Schubert, U. S. Dual hydrophilic polymers based on (meth)acrylic acid and poly(ethylene glycol) - Synthesis and water uptake behavior. *Polymer Chemistry* **2010**, *1*, 1669–1676.

(25) Schmidt, B. V. K. J. Hydrophilic polymers. *Polymers* **2019**, *11*, 693.

(26) Juárez Data, R. M.; Mattea, F.; Strumia, M. C.; Milanesio, J. M. Effect of including a hydrophobic comonomer on the rheology of an acrylamide-acrylic acid based copolymer. *Journal of Applied Polymer Science* **2020**, *137*, 1–12.

(27) Rouxel, T.; Ji, H.; Guin, J. P.; Augereau, F.; Rufflé, B. Indentation deformation mechanism in glass: Densification versus shear flow. *Journal of Applied Physics* **2010**, *107*, 094903.

(28) Humphrey, W.; Dalke, A.; Schulten, K. VMD: Visual Molecular Dynamics. *Journal of Molecular Graphics* **1996**, *14*, 33–38.

(29) Wang, J.; Wolf, R. M.; Caldwell, J. W.; Kollman, P. A.; Case, D. A. Development and

testing of a general Amber force field. *Journal of Computational Chemistry* **2004**, *25*, 1157–1174.

(30) Wang, J.; Wang, W.; Kollman, P. A.; Case, D. A. Automatic atom type and bond type perception in molecular mechanical calculations. *Journal of Molecular Graphics and Modelling* **2006**, *25*, 247–260.

(31) Avogadro: an open-source molecular builder and visualization tool. Version 1.2.0.

(32) Hanwell, M. D.; Curtis, D. E.; Lonie, D. C.; Vandermeersch, T.; Zurek, E.; Hutchison, G. R. Avogadro: an advanced semantic chemical editor, visualization, and analysis platform. *Journal of Cheminformatics* **2012**, *4*.

(33) Wu, Y.; Tepper, H. L.; Voth, G. A. Flexible simple point-charge water model with improved liquid-state properties. *Journal of Chemical Physics* **2006**, *124*, 024503.

(34) Plimpton, S. Fast Parallel Algorithms for Short-Range Molecular Dynamics. *Journal of Computational Physics* **1995**, *117*, 1–19.

(35) Nosé, S. A unified formulation of the constant temperature molecular dynamics methods. *Journal of Chemical Physics* **1984**, *81*, 511–519.

(36) Hoover, W. G. Canonical dynamics: Equilibrium phase-space distributions. *Physical Review A* **1985**, *31*, 1695–1697.

(37) Parrinello, M.; Rahman, A. Polymorphic transitions in single crystals: A new molecular dynamics method. *Journal of Applied Physics* **1981**, *52*, 7182–7190.

(38) Shinoda, W.; Shiga, M.; Mikami, M. Rapid estimation of elastic constants by molecular dynamics simulation under constant stress. *Physical Review E* **2004**, *69*, 134103.

(39) Deserno, M.; Holm, C. How to mesh up Ewald sums. I. A theoretical and numerical comparison of various particle mesh routines. *The Journal of Chemical Physics* **1998**, *109*, 7678–7693.

(40) Rigby, D.; Roe, R.-J. Molecular dynamics simulation of polymer liquid and glass. II. Short range order and orientation correlation. *Journal of Chemical Physics* **1988**, *89*, 5280–5290.

(41) Liang, J.-J.; Cygan, R. T.; Alam, T. M. Molecular dynamics simulation of the structure and properties of lithium phosphate glasses. *Journal of Non-Crystalline Solids* **2000**, *263-264*, 167–179.

(42) Napolitano, S.; Glynos, E.; Tito, N. B. Glass transition of polymers in bulk, confined geometries, and near interfaces. *Reports on Progress in Physics* **2017**, *80*, 036602.

(43) Godey, F.; Fleury, A.; Soldera, A. Local dynamics within the glass transition domain. *Scientific reports* **2019**, *9*, 9638.

(44) Evans, D. J. 6 – Computer Simulation Algorithms. Computer Science. 1990; pp 117–165.

(45) Evans, D. J.; Morriss, G. P. Nonlinear-response theory for steady planar Couette flow. *Physical Review A* **1984**, *30*, 1528–1530.

(46) Evans, D. J.; Morriss, G. P. Non-Newtonian Molecular Dynamics. *Computer Physics Reports* **1984**, *1*, 297–343.

(47) Edberg, R.; Morriss, G. P.; Evans, D. J. Rheology of n-alkanes by nonequilibrium molecular dynamics. *Journal of Chemical Physics* **1987**, *86*, 4555–4570.

(48) Daivis, P. J.; Evans, D. J.; Morriss, G. P. Computer simulation study of the comparative rheology of branched and linear alkanes. *Journal of Chemical Physics* **1992**, *97*, 616–627.

(49) Todd, B. D.; Daivis, P. J. *Nonequilibrium Molecular Dynamics: Theory, Algorithms, and Applications*; Cambridge University Press, 2017.

(50) Kelkar, M. S.; Rafferty, J. L.; Maginn, E. J.; Siepmann, J. I. Prediction of viscosities and vapor-liquid equilibria for five polyhydric alcohols by molecular simulation. *Fluid Phase Equilibria* **2007**, *260*, 218–231.

(51) Tseng, H.-C.; Wu, J.-S.; Chang, R.-Y. Shear thinning and shear dilatancy of liquid n-hexadecane via equilibrium and nonequilibrium molecular dynamics simulations: Temperature, pressure, and density effects. *Journal of Chemical Physics* **2008**, *129*, 014502.

(52) Rainwater, J. C.; Hanley, H. J. M.; Paszkiewicz, T.; Petru, Z. Non-Newtonian flow of a model liquid between concentric cylinders. *Journal of Chemical Physics* **1985**, *83*, 339–347.

(53) Menzel, A. G.; Daivis, P. J.; Todd, B. D. Equilibrium and nonequilibrium molecular dynamics methods to compute the first normal stress coefficient of a model polymer solution. *Physical Review Fluids* **2020**, *5*, 084201.

(54) Irving, J. H.; Kirkwood, J. G. The Statistical Mechanical Theory of Transport Processes. IV. The Equations of Hydrodynamics. *Journal of Chemical Physics* **1950**, *18*, 817–829.

(55) Todd, B. D.; Evans, D. J.; Daivis, P. J. Pressure tensor for inhomogeneous fluids. *Physical Review E* **1995**, *52*, 1627–1638.

(56) Hünenberger, P. H. Thermostat Algorithms for Molecular Dynamics Simulations. *Advances in Polymer Science* **2005**, *173*, 105–149.

(57) Erpenbeck, J. J. Shear Viscosity of the Hard-Sphere Fluid via Nonequilibrium Molecular Dynamics. *Physical Review Letters* **1984**, *52*, 1333–1335.

(58) Evans, D. J.; Morriss, G. P. Shear thickening and turbulence in simple fluids. *Physical Review Letters* **1986**, *56*, 2172–2175.

(59) Delhommelle, J.; Petravic, J.; Evans, D. J. Reexamination of string phase and shear thickening in simple fluids. *Physical Review E* **2003**, *68*, 031201.

(60) Braga, C.; Travis, K. P. A configurational temperature Nosé-Hoover thermostat. *Journal of Chemical Physics* **2005**, *123*, 134101.

(61) Travis, K. P.; Braga, C. Configurational temperature control for atomic and molecular systems. *Journal of Chemical Physics* **2008**, *128*, 014111.

(62) Travis, K. P.; Daivis, P. J.; Evans, D. J. Thermostats for molecular fluids undergoing shear flow: Application to liquid chlorine. *Journal of Chemical Physics* **1995**, *103*, 10638.

(63) Travis, K. P.; Daivis, P. J.; Evans, D. J. Computer simulation algorithms for molecules undergoing planar Couette flow: A nonequilibrium molecular dynamics study. *Journal of Chemical Physics* **1995**, *103*, 1109–1118.

(64) Travis, K. P.; Daivis, P. J.; Evans, D. J. Erratum: Thermostats for molecular fluids undergoing shear flow: Application to liquid chlorine [J. Chem. Phys. 103 , 10638 (1995)]. *Journal of Chemical Physics* **1996**, *105*, 3893–3894.

(65) Matin, M. L.; Daivis, P. J.; Todd, B. D. Comparison of planar shear flow and planar elongational flow for systems of small molecules. *Journal of Chemical Physics* **2000**, *113*, 9122–9131.

(66) Daivis, P. J.; Matin, M. L.; Todd, B. D. Nonlinear shear and elongational rheology of model polymer melts by non-equilibrium molecular dynamics. *Journal of Non-Newtonian Fluid Mechanics* **2003**, *111*, 1–18.

(67) Daivis, P. J.; Matin, M. L.; Todd, B. D. Nonlinear shear and elongational rheology of model polymer melts at low strain rates. *Journal of Non-Newtonian Fluid Mechanics* **2007**, *147*, 35–44.

(68) Lees, A. W.; Edwards, S. F. The computer study of transport processes under extreme conditions. *Journal of Physics C: Solid State Physics* **1972**, *5*, 1921–1928.

(69) Hess, S. Non-Newtonian viscosity and normal pressure differences of simple liquids. *Physical Review A* **1982**, *25*, 614–616.

(70) Hess, S.; Hanley, H. J. M. Distortion of the structure of a simple fluid. *Physical Review A* **1982**, *25*, 1801–1804.

(71) Hess, S. Similarities and differences in the nonlinear flow behavior of simple and of molecular liquids. *Physica A* **1983**, *118*, 79–104.

(72) Bird, B. R.; Armstrong, R. C.; Hassager, O. *Dynamics of Polymeric Fluids, Volume 1: Fluid Mechanics*; John Wiley and Sons: New York, 1987; Vol. 1.

(73) Kröger, M. *Models for Polymeric and Anisotropic Liquids*; Lecture Notes in Physics; Springer Berlin Heidelberg, 2005.

(74) Evans, D. J.; Sarman, S. Equivalence of Thermostatted Nonlinear Responses. *Physical Review E* **1993**, *48*, 65.

(75) Poole, R. J. The Deborah and Weissenberg numbers. *Rheology Bulletin* **2012**, *53*, 32–39.

(76) Burshtein, N.; Zografos, K.; Shen, A. Q.; Poole, R. J.; Haward, S. J. Inertioelastic Flow Instability at a Stagnation Point. *Physical Review X* **2017**, *7*, 041039.

(77) O'Sullivan, T. J.; Kannam, S. K.; Chakraborty, D.; Todd, B. D.; Sader, J. E. Viscoelasticity of liquid water investigated using molecular dynamics simulations. *Physical Review Fluids* **2019**, *4*, 123302.

(78) Smith, P. E.; van Gunsteren, W. F. The viscosity of SPC and SPC/E water at 277 and 300 K. *Chemical Physics Letters* **1993**, *215*, 315–318.

(79) Barnes, H. A. The yield stress - a review - everything flows? *Journal of Non-Newtonian Fluid Mechanics* **1999**, *81*, 133–178.

(80) Møller, P. C. F.; Fall, A.; Bonn, D. Origin of apparent viscosity in yield stress fluids below yielding. *Europhysics Letters* **2009**, *87*, 38004.

(81) Bonn, D.; Denn, M. M. Yield Stres Fluids Slowly Yield to Analysis. *Science* **2009**, *324*, 1401–1403.

(82) Walls, H. J.; Caines, S. B.; Sanchez, A. M.; Khan, S. A. Yield stress and wall slip phenomena in colloidal silica gels. *Journal of Rheology* **2003**, *47*, 847–868.

(83) Yasuda, K. A Multi-Mode Viscosity Model and Its Applicability to non-Newtonian Fluids. *Journal of Textile Engineering* **2006**, *52*, 171–173.

(84) Rao, M. A. *Rheology of Fluid and Semisolid Foods Principles and Applications*; Springer US, 2007; Chapter 2. Flow and Functional Models for Rheological Properties of Fluid, pp 27–58.

(85) Poslinski, A. J.; Ryan, M. E.; Gupta, R. K.; Seshadri, S. G.; Frechette, F. J. Rheological Behavior of Filled Polymeric Systems I. Yield Stress and Shear-Thinning Effects. *Journal of Rheology* **1988**, *32*, 703–735.

(86) Rainwater, J. C.; Hanley, H. J. M. Non-Newtonian flow between concentric cylinders and the effects of finite compressibility. *International Journal of Thermophysics* **1985**, *6*, 595–605.

(87) Soper, A. K. The radial distribution functions of water and ice from 220 to 673 K and at pressures up to 400 MPa. *Chemical Physics* **2000**, *258*, 121–137.

(88) Futamura, R.; Iiyama, T.; Takasaki, Y.; Gogotsi, Y.; Biggs, M. J.; Salanne, M.; Ségalini, J.; Simon, P.; Kaneko, K. Partial breaking of the Coulombic ordering of ionic liquids confined in carbon nanopores. *Nature Materials* **2017**, *16*, 1225–1232.

(89) Headen, T. F.; Boek, E. S.; Jackson, G.; Totton, T. S.; Müller, E. A. Simulation of Asphaltene Aggregation through Molecular Dynamics: Insights and Limitations. *Energy and Fuels* **2017**, *31*, 1108–1125.

(90) Mustan, F.; Ivanova, A.; Madjarova, G.; Tcholakova, S.; Denkov, N. Molecular Dynamics Simulation of the Aggregation Patterns in Aqueous Solutions of Bile Salts at Physiological Conditions. *Journal of Physical Chemistry B* **2015**, *119*, 15631–15643.

(91) Totton, T. S.; Misquitta, A. J.; Kraft, M. A quantitative study of the clustering of polycyclic aromatic hydrocarbons at high temperatures. *Phys. Chem. Chem. Phys.* **2012**, *14*, 4081–4094.

(92) Stukowski, A. Visualization and analysis of atomistic simulation data with OVITO - the Open Visualization Tool. *Modelling and Simulation in Materials Science and Engineering* **2010**, *18*, 015012.

Graphical TOC Entry